3-11-2011

A Simple Non-Destructive Method for Characterizing Non-Dispersive, Low-Loss Dielectrics

Thomas S. Olney

A SIMPLE NON-DESTRUCTIVE METHOD FOR CHARACTERIZING NON-DISPERSIVE, LOW-LOSS DIELECTRICS

THESIS

Thomas S. Olney, Captain, USAF

AFIT/GE/ENG/11-31

DEPARTMENT OF THE AIR FORCE
AIR UNIVERSITY
AIR FORCE INSTITUTE OF TECHNOLOGY

Wright-Patterson Air Force Base, Ohio

AFIT/GE/ENG/11-31

A SIMPLE NON-DESTRUCTIVE METHOD FOR CHARACTERIZING NON-DISPERSIVE, LOW-LOSS DIELECTRICS

THESIS

Presented to the Faculty

Department of Electrical and Computer Engineering

Graduate School of Engineering and Management

Air Force Institute of Technology

Air University

Air Education and Training Command

In Partial Fulfillment of the Requirements for the

Degree of Master of Science in Electrical Engineering

Thomas S. Olney, BS

Captain, USAF

March 2011

AFIT/GE/ENG/11-31

A SIMPLE NON-DESTRUCTIVE METHOD FOR CHARACTERIZING NON-DISPERSIVE, LOW-LOSS DIELECTRICS

Thomas S. Olney, BS

Captain, USAF

Approved:

Michael Havrilla Dr. Michael Havrilla (Chairman)	02 Mar 2011 Date
Michael Saville Michael Saville, Maj, USAF (Member)	2 Mar 2011 Date
Milo Hyde Milo Hyde, Capt, USAF (Member)	2 Mar 2011 Date
William P. Baker Dr. William Baker (Member)	2 Mar 2011 Date

Abstract

It is shown how permittivity can be extracted via time domain reflection data from a perfect electric conductor (PEC) backed planar sample of a low-loss, non-dispersive dielectric using two rectangular Ku-band waveguide aperture probes with attached PEC flange plates of the same geometry but different dimensions. Of critical importance is being able to identify the reflection from the edge of the flange plate in the parallel plate region created by the plate and the PEC backing of the sample. A signal processing method that takes advantage of physical insight into the geometry and superposition is developed for identifying this edge reflection.

Measurements are taken using square and circular plate geometries. Measured data is processed using both a Kaiser window and the signal subtraction method developed in this research to verify the analysis. Final results are presented and future work is discussed.

Acknowledgments

To my waterbear, my friends, and my family. Without you, I would not have been able to make it through the personal and professional challenges of the past 18 months.

I would also like to thank my advisor, without his guidance, I would still be lost in the math of electromagnetics without ever understanding the beauty behind what is physically going on.

To the yeomen of the world without whom the work would be left undone.

Thomas S. Olney

Table of Contents

Page

LIST OF FIGURES

Page

List of Tables

Page

A Simple Non-Destructive Method for Characterizing Non-Dispersive, Low-Loss Dielectrics

1. Introduction

Material characteristics define how forces interact with matter. Within the realm of electromagnetics (EM), electric and magnetic forces interact with media resulting in conduction, polarization and magnetization currents. These current densities are directly related to conductivity, permittivity and permeability respectively.

The exploitation of these parameters has been instrumental in modern technology. Being able to control how electromagnetic fields interact with a specific material has proven to be useful in applications ranging from communications to cooking. In order to make material parameters useful in applications, it often becomes of critical importance to ensure that the constitutive parameters are within specified tolerances. In order to assess the permittivity and permeability (and corresponding tolerances) of a material, a variety of parameter extraction techniques have been developed over the years. However, a large portion of these methods are either destructive to the material under test, computationally demanding or both. This leads to increased cost since there is time lost in sample preparation, testing and computation of the constitutive parameters. However, methods that can provide non-destructive, computationally simple ways to determine the constructive parameters, even if limited to just determining the permittivity of a material, would be of enormous benefit as it would cut costs without sacrificing quality.

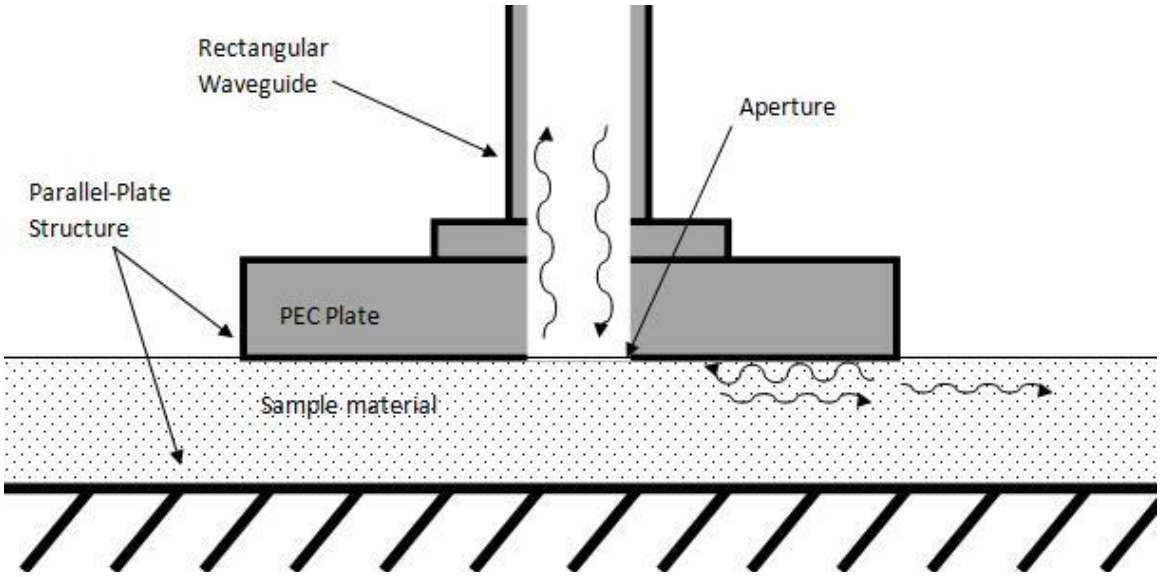

Figure 1-1. Basic setup of probe

1.1 Problem Statement

As previously stated, a majority of methods for characterizing the parameters of a material are destructive, computationally demanding or both. In most cases, in order to save time using computational resources, a closed form method for determining permittivity and permeability is used. One common method is the Nicholson Ross Weir (NRW) algorithm [2], [6], [16]. The NRW method uses an exact formulation to find the complex permittivity and permeability of a material; however, it is a destructive method. This means that the material under test has to be machined to fit in the waveguide sample holder. This comes with two drawbacks, namely, a limited sample interrogation area and the added time associated with sample preparation.

The goal of this thesis is to develop a new, computationally efficient, non-destructive method for characterizing a material using a simple time domain technique. In this new technique, reflections from the aperture and the edges of a flanged rectangular

waveguide probe are utilized to extract the complex permittivity of a conductor backed dielectric material as depicted in Figure 1-1.

1.2 Limitations

The time-domain analysis technique introduced in this research does have some limitations. First, since the edge reflection from the plates must be observed, the material under test must be low loss; otherwise, the reflection would never be observed. Additionally, the material must have very low dispersion; otherwise, the temporal response may lack sufficient resolution required by the technique. Furthermore, since the network analyzer (NWA) does not collect time-domain data but uses a Fourier Transform (FT) to convert frequency-based data into the time-domain, there is a limit in resolution which is directly related to the bandwidth of the probe being used to make the measurements.

Other tradeoffs are made by using only reflection measurements. Since, as a rule of thumb, one can only solve for as many unknowns as measurements taken, it becomes apparent that either the permittivity or permeability can be computed, but not both.

1.3 Scope

Many methods are available for measuring the constitutive parameters of a material. However, the focus of this thesis will be on using waveguide probes. As mentioned before, the bandwidth limits the resolution in the time domain. Therefore, Ku Band waveguides have been selected for use. This decision was based on two factors. First, the NWA used in this research only has a range from 10.0MHz to 20.0GHz, and secondly, within that range, the Ku Band provides the largest bandwidth for a waveguide,

covering from 10.0GHz to 18.5GHz. A full development of how this bandwidth was calculated is located in appendix C. Additionally, since both constitutive parameters cannot be simultaneously computed, the scope will be limited to non-magnetic materials (i.e., dielectrics). While the scope has been limited to these conditions, the overall analysis will be accomplished in a way that could be applied to other probe devices with different bandwidths.

1.4 Thesis Organization

Chapter 2 provides a theoretical background starting with Maxwell's equations and constitutive parameters, then discusses wave behavior in parallel plate systems before finishing with calibration of the waveguide system. Chapter 3 introduces the measurement setup and calibration scheme, develops a method for processing the raw data retrieved from the NWA, and discusses how the processed data is utilized by the new technique for extracting complex permittivity. Chapter 4 covers the uncertainty associated with the measurement system, presents data gathered from measuring Plexiglas samples of different thicknesses, uses the processed data to extract relative complex permittivity and compares the results against known standards. Chapter 5 contains conclusions as well as recommendations for future work.

2. Background

Since the probe used in this research involves a parallel-plate structure, a field analysis of this guide is required to understand the wave propagation behavior which is necessary for the material extraction technique introduced in this work. First, Maxwell's Equations are reviewed, and a specialized formulation for this research is given. Then a Green's function, vector potential technique is briefly reviewed. Next the practical aspect of probe calibration is discussed due to its importance in obtaining accurate/reliable experimental measurements for comparison to the Green's function based theoretical parameter extraction model. Lastly, the key points of this chapter are summarized.

2.1 Maxwell's Equations and Constitutive Parameters

The derivation for this section is drawn from Balanis [4] and Harrington [12]. Maxwell's equations in time harmonic form with an assumed and suppressed $e^{j\omega t}$ time dependence are given by

$$\nabla \times \bar{E} = -\bar{M}_i - j\omega\bar{B} \tag{2-1}$$

$$\nabla \times \bar{H} = \bar{J}_i + \bar{J}_c + j\omega\bar{D} \tag{2-2}$$

$$\nabla \bullet \bar{D} = q_{ev} \tag{2-3}$$

$$\nabla \bullet \bar{B} = q_{mv} \tag{2-4}$$

where $\overline{\mathrm{E}}$ represents the electric field intensity; $\overline{\mathrm{H}}$ is the magnetic field intensity; $\overline{\mathrm{D}}$ is the electric flux density; $\overline{\mathrm{B}}$ is the magnetic flux density; $\bar{\mathrm{J}}$ is the electric current density, and $\overline{\mathrm{M}}$ is the magnetic current density. In both cases, the subscript "i" represents the impressed or source current, while with electric currents, the subscript "c" represents the conduction current density. Finally, q_{ev} is the electric charge density while q_{mv} is the magnetic charge density.

These equations become well posed upon utilizing the constitutive relations for simple (i.e., linear , homogeneous, isotropic) media, namely

$$\begin{aligned} \overline{\mathrm{D}}(\bar{r},\omega) &= \varepsilon(\omega)\,\overline{\mathrm{E}}(\bar{r},\omega) \\ \overline{\mathrm{B}}(\bar{r},\omega) &= \mu(\omega)\,\overline{\mathrm{H}}(\bar{r},\omega) \\ \bar{\mathrm{J}}_{\mathrm{c}}(\bar{r},\omega) &= \sigma(\omega)\,\overline{\mathrm{E}}(\bar{r},\omega). \end{aligned} \tag{2-5}$$

The previously determined scope of a low loss $(\varepsilon'' << \varepsilon')$, non-magnetic $(\mu(\omega) \to \mu_0)$, low dispersive $(\varepsilon(\omega) \to \varepsilon)$ material leads to the following specialized form of Maxwell's Equations which will be utilized in this research

$$\begin{aligned} \nabla \times \overline{\mathrm{H}} &= \bar{\mathrm{J}}_{\mathrm{i}} + \sigma\,\overline{\mathrm{E}} + j\omega\varepsilon\,\overline{\mathrm{E}} \\ &= \bar{\mathrm{J}}_{\mathrm{i}} + j\omega\left(\varepsilon + \frac{\sigma}{j\omega}\right)\overline{\mathrm{E}} \end{aligned} \tag{2-6}$$

$$\varepsilon_c = \left(\varepsilon - j\frac{\sigma}{\omega}\right) = \varepsilon_0(\varepsilon' - j\varepsilon''). \tag{2-7}$$

2.2 Green's Function and Vector Potentials in a Parallel-Plate Region

The rigorous formulation of the transverse fields inside the parallel plate region is found by replacing the waveguide aperture with a magnetic current in accordance with

Love's equivalence principle [11]. This transverse magnetic field can be found by utilizing the following relation [4], [8]

$$\overline{\mathrm{H}}_t^{pp} = \frac{1}{j\omega\varepsilon\mu}\left(k^2 + \nabla_t\nabla\bullet\right)\overline{\mathrm{F}}. \tag{2-8}$$

where ∇_t is the transverse gradient operator,

$$\nabla_t = \hat{x}\frac{\partial}{\partial x} + \hat{y}\frac{\partial}{\partial y}, \tag{2-9}$$

and the electric vector potential $\overline{\mathrm{F}}$ is given as

$$\overline{\mathrm{F}} = \int_0^b\int_0^a \ddot{\mathrm{G}}(x,y,z \mid x',y',0)\bullet\varepsilon\overline{\mathrm{M}}(x',y')dx'dy' \tag{2-10}$$

where *b* and *a* are the aperture dimensions, and $\ddot{\mathrm{G}}$ is the rectangular form of the dyadic, parallel-plate Green's function. $\ddot{\mathrm{G}}$ is derived by Hanson and Yakovlev [5], [8] as

$$\ddot{\mathrm{G}} = \hat{x}\mathrm{G}_t\hat{x} + \hat{\mathrm{y}}\mathrm{G}_t\hat{\mathrm{y}} + \hat{\mathrm{z}}\mathrm{G}_t\hat{\mathrm{z}} \tag{2-11}$$

$$\mathrm{G}_{\mathrm{t,n}} = \frac{1}{(2\pi)^2}\int_{-\infty}^{\infty}\int_{-\infty}^{\infty} g_{t,n}(\xi,\eta;z \mid z')e^{j\xi(x-x')}e^{j\eta(y-y')}d\xi d\eta \tag{2-12}$$

$$g_{t,n} = \frac{\cosh p\left(d-\mid z-z'\mid\right)\pm\cosh p\left(d-\mid z+z'\mid\right)}{2p\sinh pd}. \tag{2-13}$$

where *d* is the sample material thickness; ξ and η are the Fourier pairs for x and y respectively; the subscript "*t*" and "*n*" identify the transverse and normal components of the Green's function respectively; and the z-directed wave number for the rectangular form is $p = \sqrt{\xi^2+\eta^2-k^2}$ [8].

However, in order to gain full insight into the wave behavior in the parallel-plate region, the polar form must be examined. Substituting $x - x' = R\cos\theta$, $y - y' = R\sin\theta$, $\xi = \lambda\cos\phi$, and $\eta = \lambda\sin\phi$ into (2-12) yields

$$\mathrm{G}_{\mathrm{t,n}} = \frac{1}{(2\pi)^2}\int_0^{\infty}\lambda g_{t,n}(\lambda; z \mid z')\int_{-\pi}^{\pi} e^{j\lambda R\cos(\phi-\theta)}d\phi d\lambda \tag{2-14}$$

where $\lambda = \sqrt{\xi^2 + \eta^2}$ and the distance from the source to the observation point is $R = \left|\bar{\rho} - \bar{\rho}'\right|$. Furthermore, the z-directed wave number is now defined as $p = \sqrt{\lambda^2 - k^2}$. Closer examination of the integral with respect to ϕ reveals it to have a well known solution of $2\pi J_0(\lambda R)$. Using that solution with the Bessel-Hankel Function relation, $J_0(z) = \frac{1}{2}\left[H_0^{(1)}(z) + H_0^{(2)}(z)\right]$, and the analytic continuation formula, $H_0^{(2)}(z) = -H_0^{(1)}(-z)$, (2-14) can now be defined as

$$\mathrm{G}_{\mathrm{t,n}} = \frac{1}{4\pi}\int_{-\infty}^{\infty}\lambda g_{t,n}(\lambda; z \mid z')H_0^{(2)}(\lambda R)d\lambda \quad . \tag{2-15}$$

Using the complex plane analysis found in [8], the polar form for (2-15) is found to be

$$\mathrm{G}_{\mathrm{t,n}} = \frac{-j}{4d(1+\delta_{l,0})}H_0^{(2)}(\lambda_l R)\bullet\left[\cos\left(\frac{l\pi}{d}|z-z'|\right) \pm \cos\left(\frac{l\pi}{d}|z+z'|\right)\right] \tag{2-16}$$

where l is the parallel-plate mode number; $\lambda_l = \sqrt{k^2 - (l\pi/d)^2}$; and $\delta_{l,0} = 1$ for $l = 0$ and $\delta_{l,0} = 0$ for $l \neq 0$. Realizing that $l = 0$ is both non-trivial and the dominant mode, several key insights into the wave behavior inside the parallel-plate region can be made. First, in the 0^{th} order dominate mode, the propagation constant is $\lambda_0 = k = \omega\sqrt{\varepsilon\mu_0}$. Secondly, since the second order Hankel function can be approximated in the far-field as

$$H_0^{(2)}(\lambda R) \sim \sqrt{\frac{2j}{\pi\lambda R}} e^{-j\lambda R}, \tag{2-17}$$

the radial field behavior in the far-field of the parallel plate region is proportional to $e^{-j\lambda R}$ [8]. Understanding the far-field behavior is necessary to the development of this method since an accurate characterization of the edge reflection, which is considered to occur in the far-field, is necessary for its use in parameter extraction.

2.3 Calibration of the Network Analyzer

In order to take accurate measurements using a parallel plate system, rather complicated calibration is often necessary [3]. Calibration complexity is increased by the use of a rectangular waveguide probe which is non-standard for the NWA. Therefore, in order to properly design a calibration method for the rectangular waveguide probe, it is necessary to understand how the more common calibrations are accomplished.

In order to fully correct for all of the errors that the NWA may detect within a system it is necessary to perform what is known as a full two-port calibration. Typically, this is accomplished via one of two methods utilizing different calibrations standards. The first is the Short-Open-Load-Thru (SOLT) method, and the second is the Thru-Reflect-Line (TRL) technique. The latter (which is employed in this research) is commonly used in noncoaxial systems due to the ease of fabrication for the standards [6].

The mathematical model that relates the S-parameters of the device under test (S_{11}^s, S_{21}^s, S_{22}^s, S_{12}^s) to the S-parameters measured by the NWA detectors (S_{11}^{ms}, S_{21}^{ms}, S_{22}^{ms}, S_{12}^{ms}) is given by [6]

$$S_{11}^{ms} = S_{11}^{A} + \frac{S_{21}^{A} S_{12}^{A} \left(S_{11}^{s} + \dfrac{S_{21}^{s} S_{12}^{s} S_{11}^{B}}{1 - S_{22}^{s} S_{11}^{B}} \right)}{1 - S_{22}^{A} \left(S_{11}^{s} + \dfrac{S_{21}^{s} S_{12}^{s} S_{11}^{B}}{1 - S_{22}^{s} S_{11}^{B}} \right)}$$

$$S_{21}^{ms} = S_{21}^{ct} + \frac{S_{21}^{A} S_{21}^{B} S_{21}^{s}}{\left[1 - S_{22}^{A} \left(S_{11}^{s} + \dfrac{S_{21}^{s} S_{12}^{s} S_{11}^{B}}{1 - S_{22}^{s} S_{11}^{B}} \right) \right] \left(1 - S_{22}^{s} S_{11}^{B} \right)}. \qquad (2\text{-}18)$$

$$S_{22}^{ms} = S_{22}^{B'} + \frac{S_{12}^{B'} S_{21}^{B'} \left(S_{22}^{s} + \dfrac{S_{12}^{s} S_{21}^{s} S_{22}^{A'}}{1 - S_{11}^{s} S_{22}^{A'}} \right)}{1 - S_{11}^{B'} \left(S_{22}^{s} + \dfrac{S_{12}^{s} S_{21}^{s} S_{22}^{A'}}{1 - S_{11}^{s} S_{22}^{A'}} \right)}$$

$$S_{21}^{ms} = S_{12}^{ct'} + \frac{S_{12}^{B'} S_{12}^{A'} S_{12}^{s}}{\left[1 - S_{11}^{B'} \left(S_{22}^{s} + \dfrac{S_{12}^{s} S_{21}^{s} S_{22}^{A'}}{1 - S_{11}^{s} S_{22}^{A'}} \right) \right] \left(1 - S_{11}^{s} S_{22}^{A'} \right)}$$

A careful examination of these equations reveals that there are 12 unknowns (S_{11}^{A}, S_{22}^{A}, $S_{22}^{A'}, S_{11}^{B}$, $S_{22}^{B'}, S_{11}^{B'}$, $S_{11}^{ct}, S_{22}^{ct'}, S_{21}^{A} S_{12}^{A}$, $S_{21}^{A} S_{21}^{B}$, $S_{12}^{B'} S_{21}^{B'}$, and $S_{12}^{B'} S_{12}^{A'}$). In the TRL technique [6], a Thru

$$\text{Thru} = \begin{bmatrix} S_{11}^{s} & S_{12}^{s} \\ S_{21}^{s} & S_{22}^{s} \end{bmatrix} = \begin{bmatrix} 0 & 1 \\ 1 & 0 \end{bmatrix}, \qquad (2\text{-}19)$$

Reflect

$$\text{Reflect} = \begin{bmatrix} S_{11}^{s} & S_{12}^{s} \\ S_{21}^{s} & S_{22}^{s} \end{bmatrix} = \begin{bmatrix} 1 & 0 \\ 0 & 1 \end{bmatrix}. \qquad (2\text{-}20)$$

and Line

$$\text{Line} = \begin{bmatrix} S_{11}^{s} & S_{12}^{s} \\ S_{21}^{s} & S_{22}^{s} \end{bmatrix} = \begin{bmatrix} 0 & 1e^{-jk_0 d} \\ 1e^{-jk_0 d} & 0 \end{bmatrix} \tag{2-21}$$

standard (in addition to other assumptions) are utilized to solve for the error terms in the calibration model. Once these error terms are determined, the desired S-parameters of the sample measurement can be accurately computed using the NWA processor.

2.4 Summary

In this chapter, a brief review of EM theory was provided. Additionally, the wave behavior inside a parallel plate system was discussed. This characterization provides the foundation of the mathematical assumptions made in Chapter 3. Most of the characterization was limited to the very specific example of parallel plate regions as this is a vital part of the measurement system used in this thesis. More detailed information on wave behavior and Green's functions can be found in the sources cited. Finally, a basic TRL calibration method was discussed in order to provide the background of the more specialized TRL calibration that will be developed in Chapter 3.

3. Methodology

Based on the information presented in previous chapter, a method for extracting permittivity from a non-magnetic, non-dispersive, low loss dielectric using a waveguide probe is detailed. The process includes setting up and calibrating the measurement system, determining the frequency range, processing the data, and concludes with the mathematical extraction of the permittivity from the measured and processed sample S parameters.

3.1 Measurement System Setup

The measurement system consists of several parts, as shown in Figure 3-1. The system includes a NWA, cables, Ku-band waveguides, and flange plates to be attached to the end of the waveguides. Note, although a single probe is used for material property extraction, a full 2-port TRL calibration is performed.

All flange plates contain a Ku-band sized aperture that allows for fields from the waveguide to pass through into the parallel-plate sample region. The flange plates are split into two separate geometries (circular and square) and have two different dimensions per geometry. For the circular flange plates, the diameters are 6 inches (0.1524m) and 4 inches (0.1016m). For the square flange plates, the larger ones have a length and width of 6 inches (0.1524m) while the smaller ones have a length and width of 4 inches (0.1016m). The square flange plates mimic geometries used in previous parallel plate waveguide probe work [9]. However, the circular flange plates were developed in an attempt to increase the amplitude of the response from the edge reflection. For each

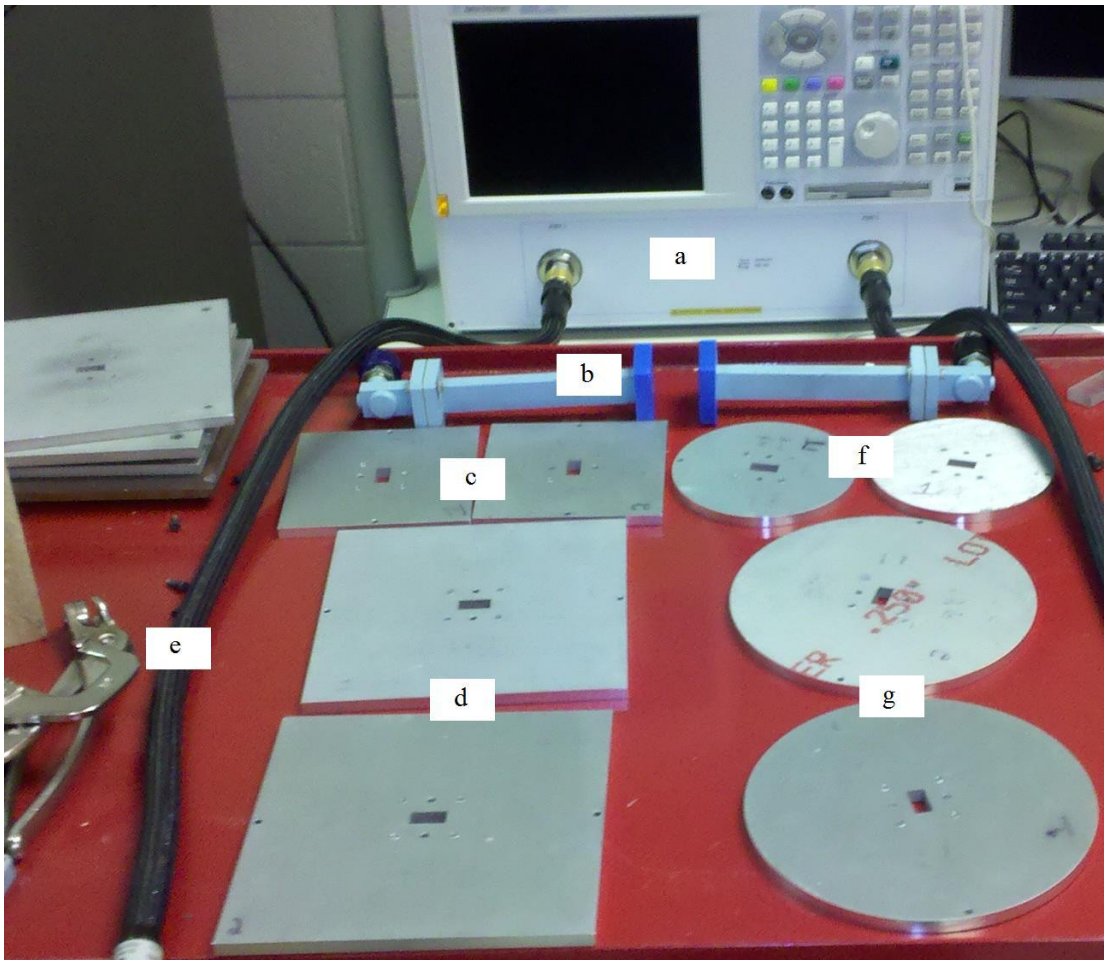

Figure 3-1: Measurement system components: (a) Network Analyzer, (b) Ku-band waveguide, (c) 4" length/width square plates, (d) 6" length/width square plates, (e) cable to connect waveguide to NWA, (f) 4" diameter circular plates, and (g) 6" diameter circular plates.

plate size and geometry, there are two plates in order to facilitate a two port TRL calibration. Drawings for the plates are located in Appendix B.

In order to setup the measurement system, a flange plate is attached to the end of the waveguide so that the apertures line up (using precision alignment pins), and the

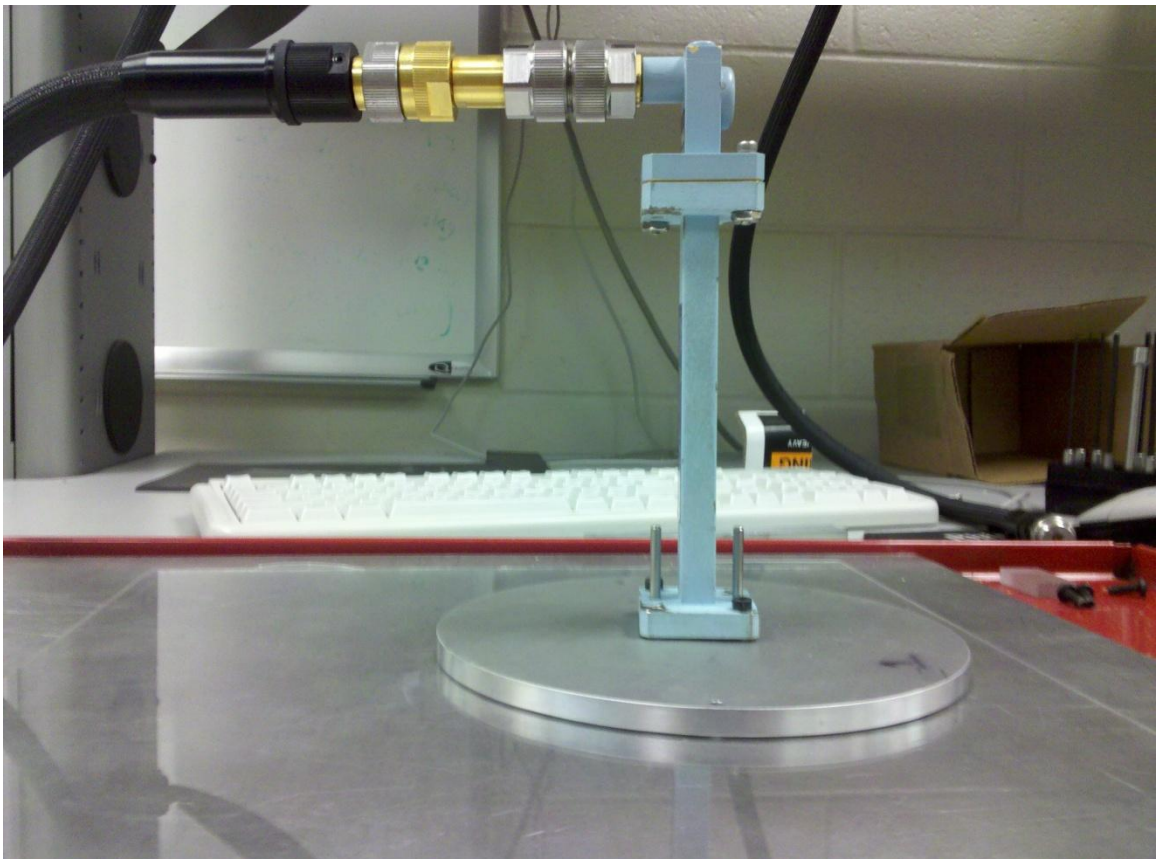

Figure 3-2: Fully connected waveguide probe.

cable is used to connect the probe to the NWA. Figure 3-2 shows a connected waveguide probe.

3.2 Calibration Details

As discussed in the previous section, there are two plates of each size and geometry in order to facilitate a two port calibration. The two port calibration, while more intensive than no calibration or a one port calibration, carries many benefits. First, a two port calibration identifies and removes errors from the measurement system. Additionally, since the system is waveguide based, the TRL method can be used. This carries the benefit of easy-to-manufacture standards [6]. Finally, and most importantly, the two port calibration allows for the reference plane to be set at the point where the

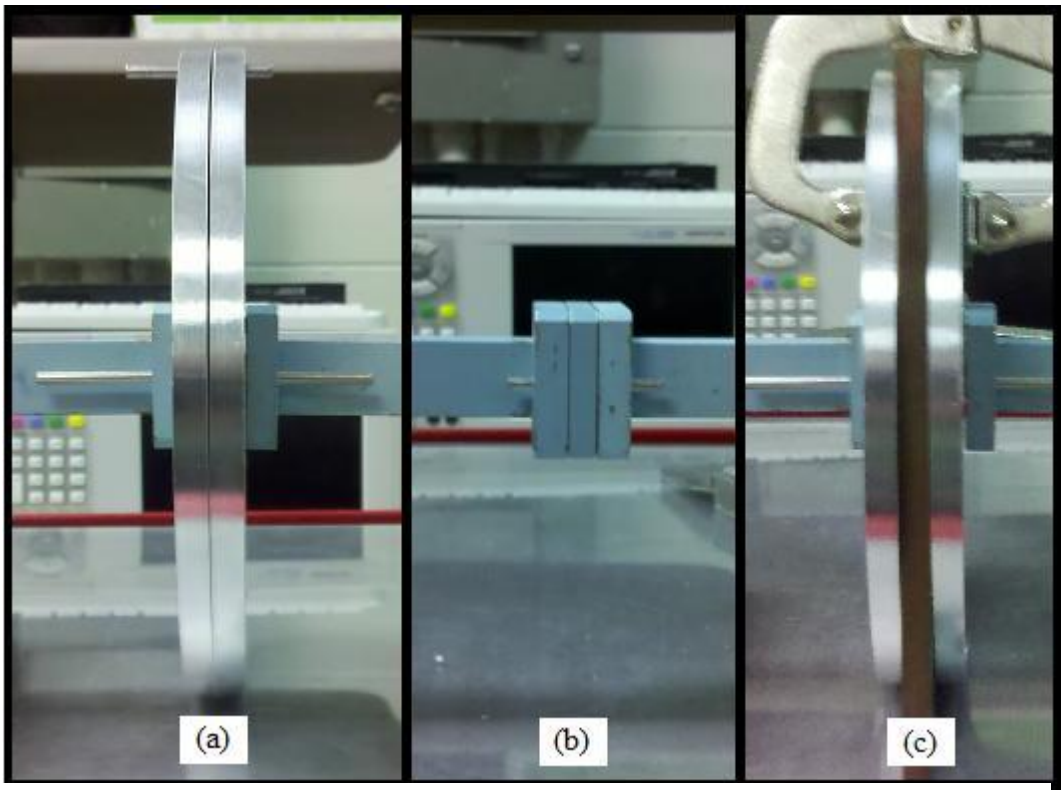

Figure 3-3: Calibration setups for the (a) thru standard, (b) line standard, and (c) reflect standard.

plate aperture meets the sample material. This means that all temporal reflections measured within the probe system will be referenced to time $t_0 = 0$.

However, because of the unique geometry associated with the parallel plate system, the two port TRL calibration has to be modified slightly. The thru standard, shown in Figure 3-3(a), is formed by joining the probes connected to each port of the NWA so that there is a single open path from one port to the other. With the two calibration planes of each probe joined up, there will be no reflections at the sample. Therefore, the S_{21}^{s} and S_{12}^{s} values will be 1 since all the energy transmitted down one waveguide will be transferred to the other. This coincides with the sample setup in (2-19).

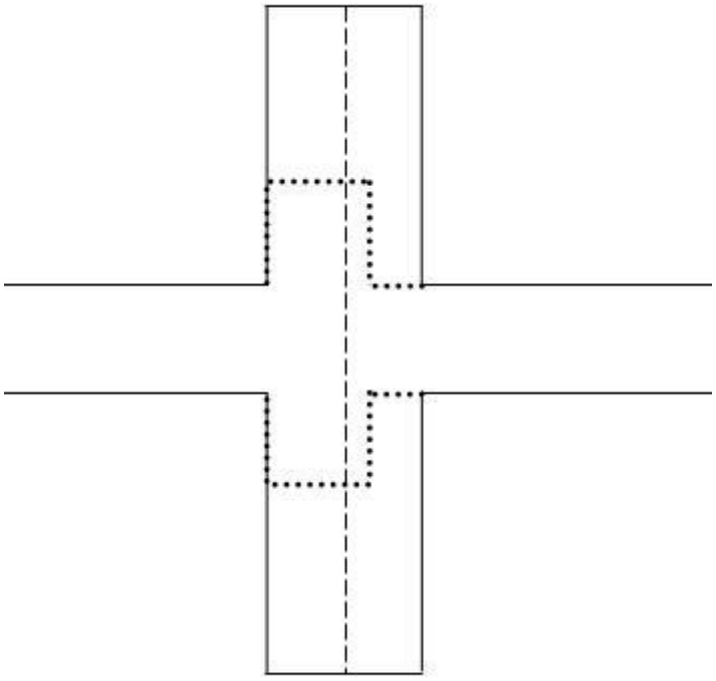

Figure 3-4: Diagram showing the size difference parallel plate thru standard setup (denoted by solid lines with a dash line separating the two probes) and the line standard (denoted by the dotted lines).

The line standard presents a tougher problem for calibration since parallel plate systems are designed to be non-destructive. However, the calibration measurement can be accomplished by using the regular waveguide line standard, shown in Figure 3-3(b). Examining (2-21) gives insight into how this is possible. In a regular waveguide calibration, the line standard measurement is calculated by using the distance between the two calibration planes as an offset in order to calculate the field's phase changes. Using this type of standard, the distance is a positive value. However, as is evident from Figure 3-4, the distance between the two reference planes is no longer positive. Therefore, if

this negative distance can be calculated, then the negative phase change can be calculated using the formula

$$\tau_d = \frac{-d}{c} = -\frac{d_{plates} - d_{LS}}{c} \tag{3-1}$$

where d_{plates} is the size of two plates stacked together and d_{LS} is the size of the regular waveguide line standard. The line standard used for the measurement system has a thickness of 6.44mm. Using this value in conjunction with (3-1), the delay time for each plate size and geometry can be calculated as shown in Table 3-1.

Table 3-1: Plate thickness measurements and associated delay time

	Meas 1 (mm)	Meas 2 (mm)	Meas 3 (mm)	Meas 4 (mm)	Avg (mm)	d (mm)	τ_d (ps)
6" Rect	13.14	13.23	13.13	13.12	13.155	6.715	-22.3988
4" Rect	13.15	13.09	13.15	13.12	13.1275	6.6875	-22.3071
6" Circ	13.17	13.12	13.10	13.13	13.13	6.69	-22.3154
4" Circ	13.16	13.14	13.14	13.15	13.1475	6.7075	-22.3738

The reflect standard is easily realized via placement of a metal plate between the probe flanges as shown in Figure 3-3(c) This coincides with the setup given in (2-20).

As a final note, when accomplishing the TRL calibration, in order to minimize the flange plate reattachment, the calibration is accomplished by doing the line standard first, then the thru and reflect standards.

3.3 Frequency Range

Prior to calibrating the NWA, the frequency range for the measurement must be set. The waveguide probe contains two structures that present limits to the frequency range. The first is the waveguide itself. A full discussion of the frequency range that the

Ku-band waveguides used in this research can cover is presented in Appendix C. The second structure is the parallel-plate region created by the flange plate and the PEC backed sample. The cutoff frequency, f_c, for parallel plate regions like these is given as

$$f_c = \frac{c}{2\sqrt{\varepsilon_r}}\left(\frac{n}{a}\right) \tag{3-2}$$

where *n* is the mode number and *a* is thickness of the sample [4]. For the 0^{th} order mode, which as discussed in Chapter 2 is dominant, $f_c = 0\text{Hz}$. However, depending on complex permittivity, sample thickness, and frequency, the 1^{st} order mode can be excited in the parallel-plate region. Once "higher order" modes are excited, the conclusions from Chapter 2 about wave behavior in the parallel-plate region are no longer valid. Since sample type and thickness may be fixed, either the theory should be modified or the upper limit of the frequency range for the system should be reduced.

Furthermore, (3-2) requires the relative complex permittivity in order to determine cutoff frequency. This presents a problem since ε_r is what is supposed to be determined by the method. As a solution to this problem, a general estimate for the cutoff frequency can be obtained heuristically by observing when the frequency-domain $S_{11}(\omega)$ measurement begins to oscillate heavily and no longer behaves in a manner similar to the lower frequency part of the measurement, that point can be estimated to be the cutoff frequency. An example of this is shown in Figure 3-5.

3.4 Data Processing

Upon completion of system calibration, conductor-backed sample measurements can be performed. This is accomplished by placing a PEC backed sample material under

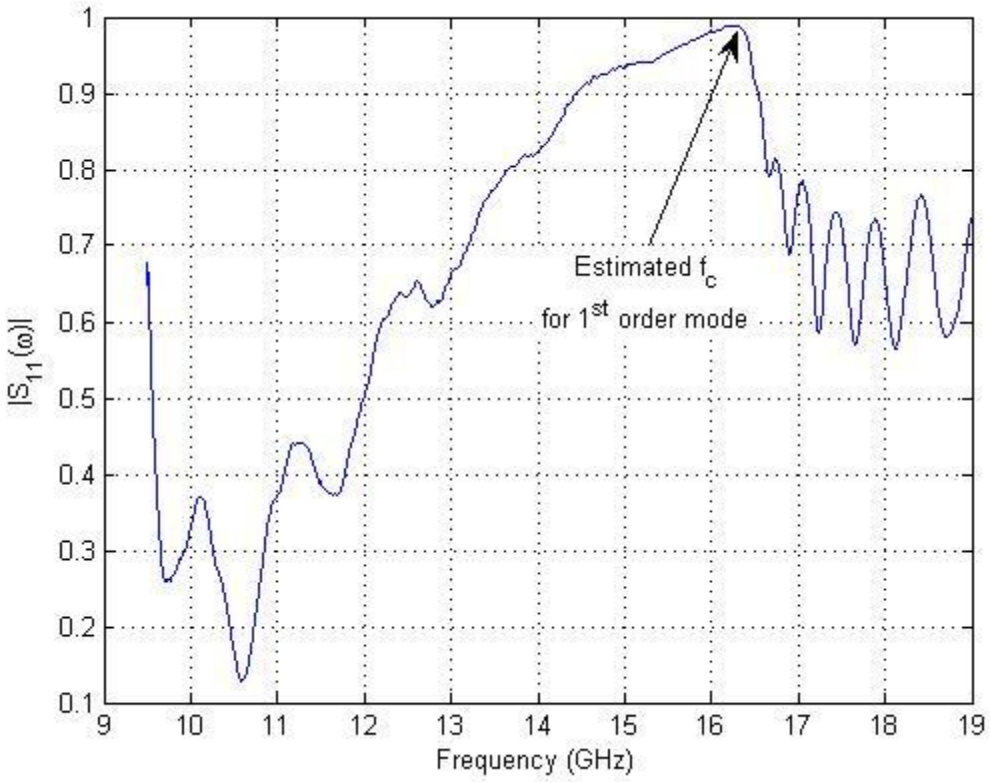

Figure 3-5: Frequency-domain data from a waveguide probe that has the 1st order mode being excited in the parallel-plate region

the probe in a setup similar to Figure 3-2 and performing a frequency swept NWA $S_{11}(\omega)$ measurement. The temporal response can be subsequently obtained via inverse Fourier transformation (i.e., IFFT) of the spectral domain response, $S_{11}(\omega)$. However, the response from the edge of the plate may not be distinguishable from the side lobes of the main reflection. An example of this is shown in Figure 3-6. Therefore, additional signal processing is necessary in order to extract the edge reflection.

In order to properly process the data, the transform processes used by the NWA must be fully understood in order to accurately extract the edge reflection from the data.

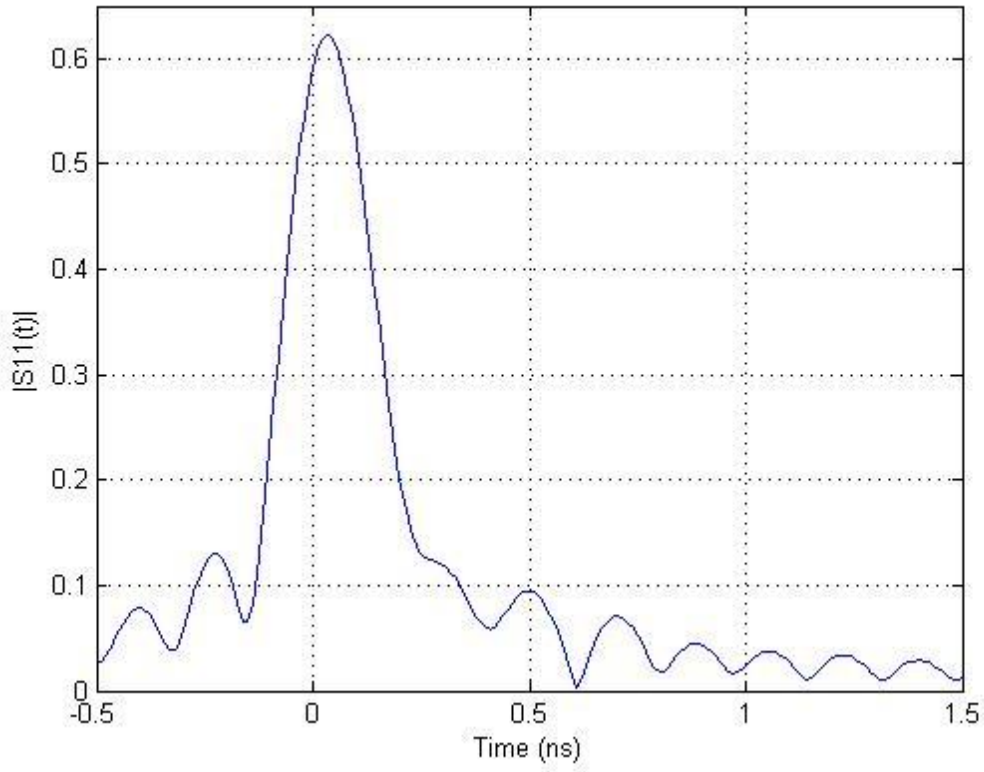

Figure 3-6: Raw time domain data of a 4" diameter circular plate

3.4.1 Fourier Analysis

A common operation performed in signal processing is the Fourier transform. Due to the discrete sampling of the measured NWA data, transforms are performed via the discrete Fourier transform (DFT). The DFT transform pair is given as

$$x(n) = \sum_{k=0}^{N-1} X[k] e^{j\frac{2\pi}{N}kn} \tag{3-3}$$

$$X[k] = \frac{1}{N} \sum_{n=0}^{N-1} x(n) e^{-j\frac{2\pi}{N}kn} \tag{3-4}$$

.

where N is the number of samples for both the frequency domain data, $X[k]$, and the time domain data, $x(n)$. Due to the inherent properties (i.e., periodic nature) of the DFT, it is of critical importance to understand the effects that finite spectral bandwidth (BW) and frequency step size (df) have on temporal resolution (T_s) and alias-free time span (T_{AF}). It is also important to understand the effect of zero-padding data (which is employed to achieve 2^N data points required by the computationally effective FFT algorithm). Using the information above, the temporal resolution, T_s, is approximately determined using the frequency step size, df , via

$$T_s \approx \frac{1}{Ndf} = \frac{1}{BW} . \tag{3-5}$$

The alias-free range for the time-domain data can be determined via $T_{AF} = NT_s$ [14].

Using the relations given above, frequency data collected from the NWA, shown in Figure 3-7(a), can be transformed into time-domain data, shown in red in Figure 3-7(b), by using the transform relations of (3-3) and (3-4). When comparing the transformed data with data gathered from the NWA, plotted in blue in Figure 3-7(b), it becomes apparent that the two graphs do not match. However, as previously stated, the data gathered from the NWA is not directly measured but the product of a Fourier analysis performed by the NWA on the frequency-domain data.

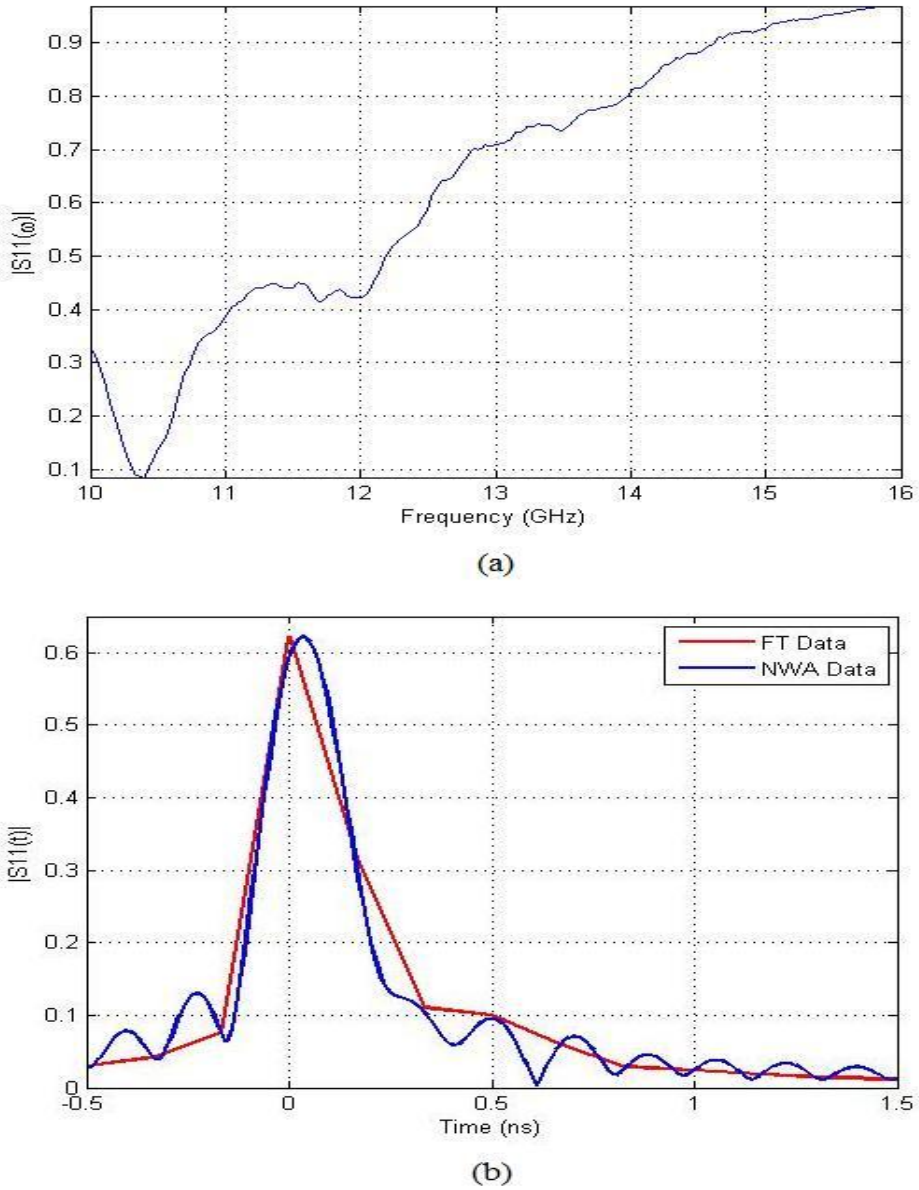

Figure 3-7: (a) Measured frequency domain data and (b) data transformed via the NWA (NWA data) and data transformed using the DFT relations of (3-3) and (3-4) (FT data) from a probe using 4 inch circular plate.

This means that some other process is at work in the NWA's Fourier analysis. The most likely reason for the apparent increase in resolution shown in the NWA data in Figure 3-7(b) is a process known as zero padding. The NWA is setup to save however

many points of data the user specifies. This is true for both frequency data and time data. Additionally, the NWA will also save the number of points for the time range specified.

As an example, if the user specifies that the NWA should have 401 points of data and sets the range for the time data to cover -2 nano-seconds (ns) to 2 ns, then the NWA will save 401 data points within that time range. However, this presents a problem. Since the NWA does not actually measure time domain data, the data displayed has to be calculated using some variation on the DFT. This means that the relation set up in (3-5) applies. Therefore, the existing number of samples has to fit into the time range determined by that relation. If this range exceeds the range set by the user in the example, then, in order for the NWA to still be able to save the user defined data points, it needs to use zero padding to increase the number of samples so that the saved data has the user defined number of points. This principle is shown in Figure 3-8 where the transformed data is zero padded until it matches the data from the NWA. The final graph shows that when 1601 data points are used for the zero pad, the computed data matches the data saved from the NWA. The large number of data points required for the zero-pad is necessary since the unpadded transformed data only had 34 data points covering the region from -2ns to 2ns. After application of the pad, the new data set now has 401 points covering the region from -2ns to 2ns.

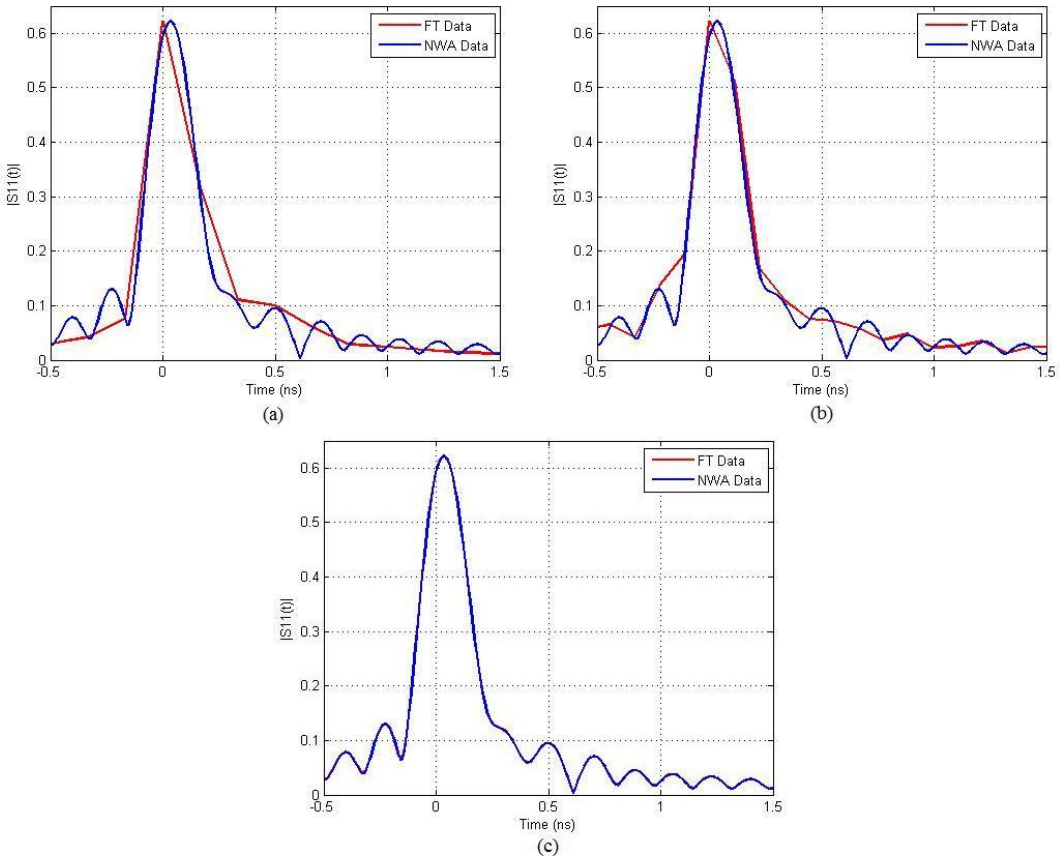

Figure 3-8: Comparison time-domain data processed by the NWA (shown in blue) with data processed using the DFT algorithm (shown in red) with a zero padding of (a) 0, (b) 101 and (c) 1601 points for a probe with a 4 inch circular plate.

3.4.2 Kaiser Windowing

After understanding the signal processing accomplished by the NWA, additional signal processing is necessary for extracting the edge response. The standard processing tool available on the NWA is a Kaiser window. The Kaiser window was chosen in this research to represent the effect of windowing functions. This decision was made since the research is designed to be a proof of concept, the application of the window will give a general idea of how similar windows affect the data. Additionally, since the Kaiser

window is a built in function of the NWA, using it maintains the simplicity of the method as no new processing algorithms are needed.

The Kaiser window is defined as

$$w(t)=\begin{cases}\dfrac{I_0\left[\beta\sqrt{1-(2t)^2}\right]}{I_0(\beta)} & |t|\le\dfrac{1}{2}\\ 0 & \text{elsewhere}\end{cases}. \tag{3-6}$$

in the time domain and

$$W(f)=\frac{\sin\left(\sqrt{\pi^2 f^2-\beta^2}\right)}{I_0(\beta)\sqrt{\pi^2 f^2-\beta^2}}. \tag{3-7}$$

in the frequency domain. In both domains, β covers a range from 0 to 10 [10]. In the Kaiser window, I_0 is a 0^{th} order modified Bessel function.

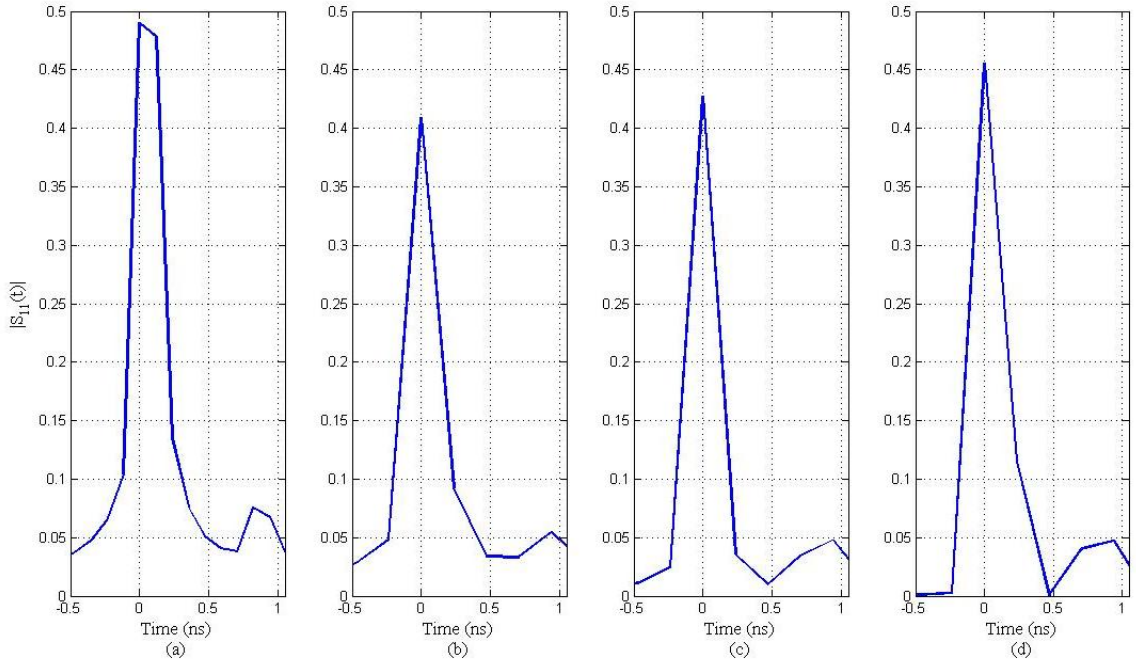

Figure 3-9: Time-domain data set with (a) no Kaiser windowing and with the following Kaiser windows applied (b) β=1, (c) β=3, and (d) β=6.

The NWA can apply the Kaiser window on using an adjustable β value in order to suppress the sidelobes of the main response so that smaller responses, like the edge reflection, become visible. An example NWA data set with no zero padding and varying β values is shown in Figure 3-9. While waveform representing the edge reflection is easily identifiable, waveform spreading is noticed. Furthermore, the peak of the edge reflection moves with the application of the window. This offset is somewhat mitigated through the use of zero-padding applied by the NWA. Therefore, when examining data with a Kaiser window applied, the results will be zero-padded.

3.4.3 Signal Subtraction

Another method for extracting the edge reflection takes advantage of the linearity of the system by using the principle of superposition to isolate the desired data. When superposition applies, it dictates that the signal, in either the frequency domain or the time domain can be broken into smaller parts that can be added together to form the original signal [14]. Therefore, by utilizing physical intuition about the system setup and how it will respond when excited, certain approximations can be employed to aid in indentifying the edge reflection signal.

The first step is to analyze the system and determine what is physically happening when it is excited. Figure 3-10(a) depicts that the EM waves reflect off of the sample and the PEC backing while other EM waves move outward away from the center. These outgoing waves will reflect off of the edge of the plate, yet not all of the waves will reflect back toward the center. Some waves will continue to head outward into the sample material. Furthermore, the waves will undergo some attenuation as they travel outward toward the edge and back. This is shown in further detail in Figure 3-11. Taking this information into account, it is relatively easy to deduce that the strongest response (the 0^{th} order reflection) will be from the initial reflection off of the PEC backing of the sample while other responses, like the edge reflection (the 1^{st} order reflection), will not be as strong when they return to the probe.

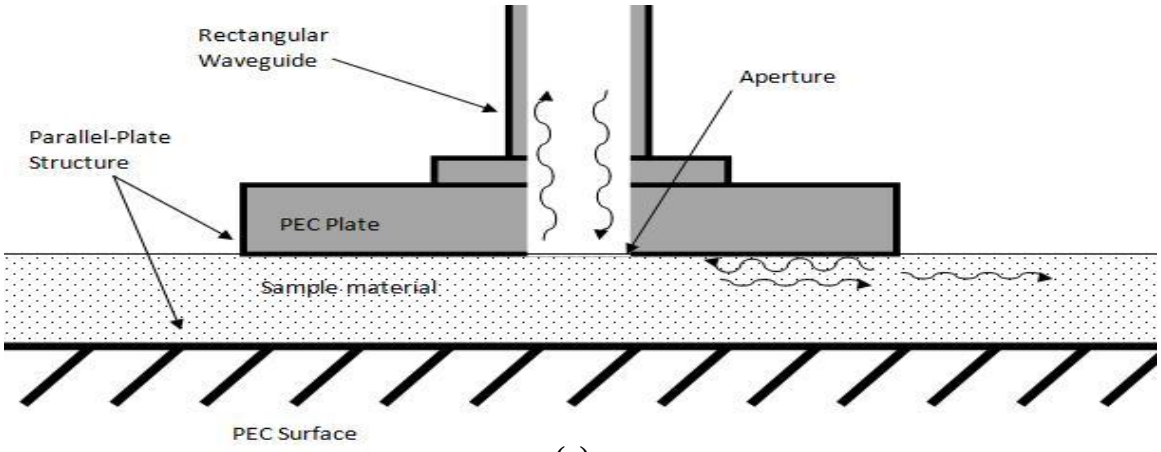

(a)

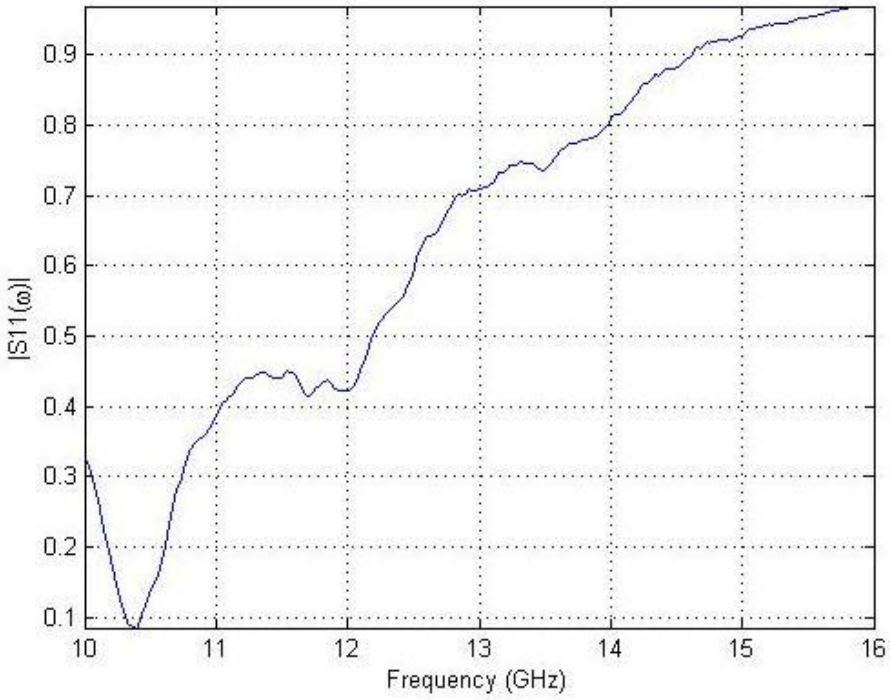

(b)

Figure 3-10: (a) Drawing showing simplified wave behavior in the measurement system and (b) measured frequency data from a probe using a 4 inch plate.

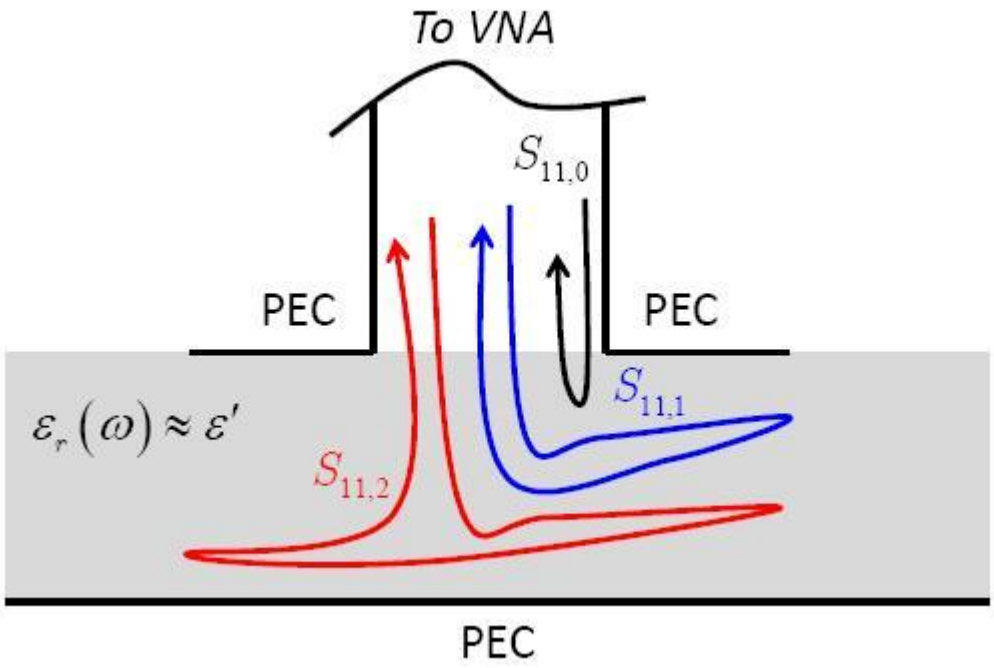

Figure 3-11: Diagram depicting the material reflection $S_{11,0}$, the first-order edge reflection $S_{11,1}$, and the second-order edge reflection $S_{11,2}$.

With this physical insight in mind, Figure 3-10(b) can be examined. Superposition says that the individual frequency responses from each scattering point will add together into the final signal in the following manner

$$S_{11}^{M}(\omega) = S_{11,0}(\omega) + S_{11,1}(\omega) + S_{11,2}(\omega) + \ldots \tag{3-8}$$

where $S_{11}^{M}(\omega)$ is the frequency-domain measured data and $S_{11,n}(\omega)$ is the n^{th} order reflection. Therefore, if there is one overly dominant response, like the 0^{th} order reflection, it will drive the basic shape of the response curve with the smaller reflections being represented as minor contributions. Based on the conclusion that the 0^{th} and 1^{st} order reflections are much stronger than the higher order reflections, (3-8) can be approximated as

$$S_{11}{}^{M}(\omega) \approx S_{11,0}(\omega) + S_{11,1}(\omega) \tag{3-9}$$

Furthermore, since $S_{11,0}(\omega) >> S_{11,1}(\omega)$, if the basic shape of $S_{11}{}^{M}(\omega)$ can be recreated via some kind of low-order polynomial fit without accounting for the minor contributions, the 0th order reflection can be approximated. The 0th order reflection, once approximated, can be subtracted from $S_{11}{}^{M}(\omega)$. Based on (3-9), this should, in effect, leave the only the 1st order response left.

Figure 3-12 illustrates how this principle works. In Figure 3-12(a), a low-order polynomial fit is applied to measured frequency-domain data. Based upon physical intuition and superposition, this fit should be an approximation of the 0th order reflection. In Figure 3-12(b), a transform is applied to the fit, and when compared to the NWA time domain data, the fit serves as a close approximation of the 0th order reflection. It should be noted that the transform conducted on the fit did not use zero padding. If the fit in Figure 3-12(b) is compared with the Fourier analysis done on the frequency data in Figure 3-8(a), the approximation is much closer. Finally, after approximating the 0th order reflection, utilizing superposition, the reflection is subtracted from the time domain data. This is shown in Figure 3-12(c). Once the 0th order reflection is removed, the only major response left is the 1st order reflection which is the edge reflection. Thus the desired delay time is now easily discernable.

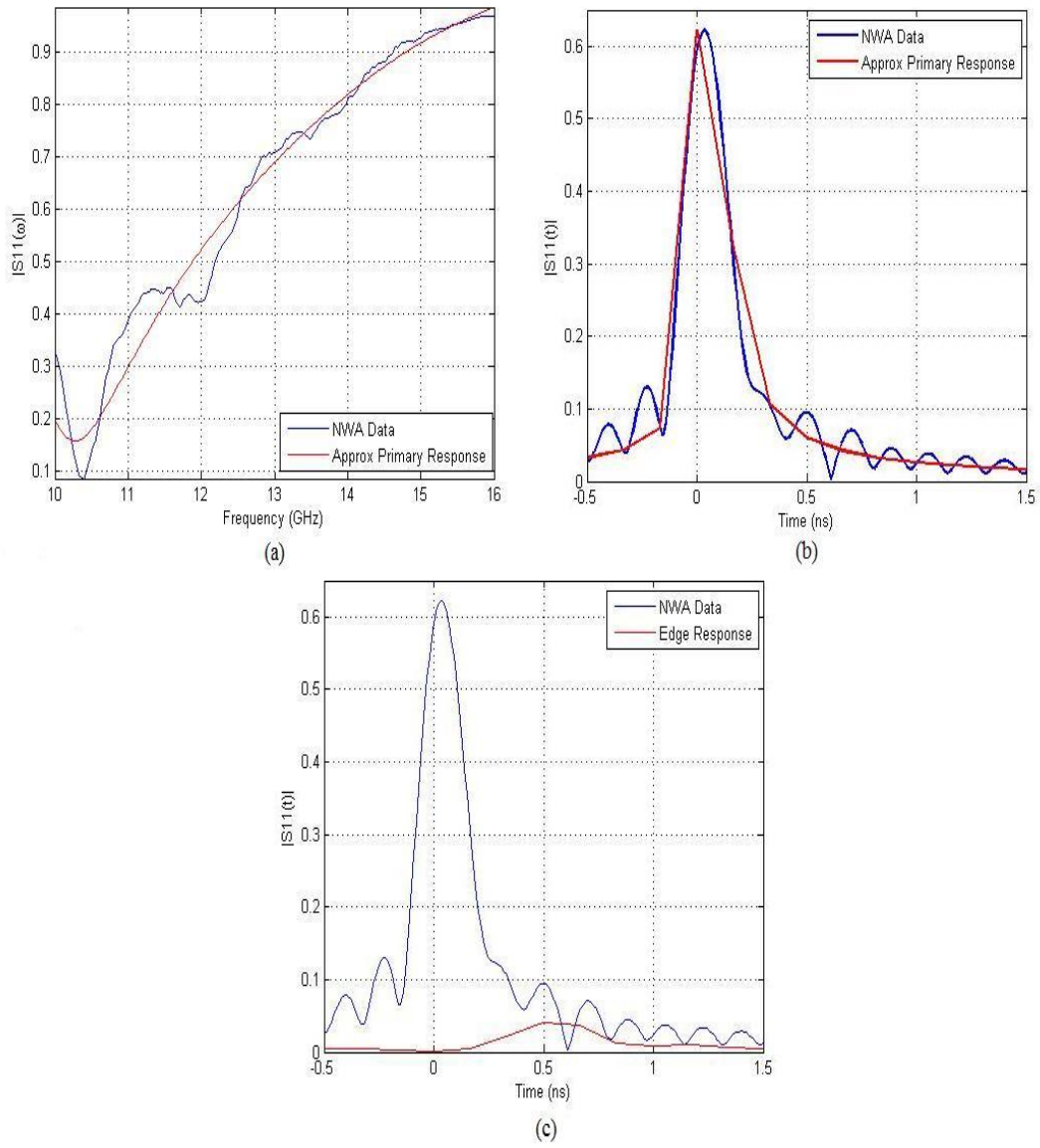

Figure 3-12: Process of performing a dominant signal subtraction: (a) a polynomial fit is applied to the frequency domain data, (b) the fit is transformed into an approximation of the 0th order reflection, and (c) the response is subtracted from the time-domain data leaving the edge reflection.

3.5 Extracting values

After isolating the edge response so that the time of its occurrence and amplitude can be determined, the permittivity can be calculated. However, in order to develop a simple extraction technique, some assumptions are made based upon the formulas reviewed in Chapter 2.

Based upon the conclusions reached via (2-16), the propagation constant, k, for the waves inside the parallel plate structure is defined as $k = \omega\sqrt{\varepsilon\mu_0} = \beta - j\alpha$ where β defines the propagation factor and α defines the attenuation factor. The phase velocity, v_p, for the wave can be calculated via the formulation

$$v_p = \frac{\omega}{\mathrm{Re}(k)} = \frac{\omega}{\beta} = v_g \tag{3-10}$$

where $\omega = 2\pi f$ is the angular frequency. Based on the information given in (3-10) and (2-7), β and α can be defined as

$$\beta = \mathrm{Re}(k) = \mathrm{Re}(\omega\sqrt{\varepsilon\mu_0}) = \mathrm{Re}\left(\omega\sqrt{\varepsilon_0\mu_0}\sqrt{\varepsilon_r}\right) = \mathrm{Re}\left(k_0\sqrt{\varepsilon_r}\right) = \mathrm{Re}(k_0\sqrt{\varepsilon' - j\varepsilon''}) \tag{3-11}$$

$$\alpha = -\mathrm{Im}(k) = -\mathrm{Im}(k_0\sqrt{\varepsilon' - j\varepsilon''}). \tag{3-12}$$

Since velocity is the ratio of distance over time, and given that the phase velocity of the waves is defined in (3-10), the time it takes for an EM wave to travel any distance in the parallel plate system can be defined as

$$t = \frac{d}{v_p}. \tag{3-13}$$

Thus, two-way travel time to the edge and back, t_{2w}, which is import for permittivity extraction, is easily computed via the formula

$$t_{2w} = \frac{d_{2w}}{v_p} \tag{3-14}$$

where d_{2w} is the distance from the center of the flange plate aperture to the flange plate edge and back.

Another relation required for permittivity extraction can be obtained by examining the attenuation that occurs. Using the previous assumption about wave behavior at the edges of the parallel plate structure, the response from the edge can be modeled as

$$V_r(t) = \frac{R}{\sqrt{k d_1^{2w}}} e^{-\alpha d_1^{2w}} e^{-j\beta d_1^{2w}}. \tag{3-15}$$

where R is a value representing the complex magnitude of the reflected energy from the edge. Since the amount of energy being lost at the edges is not known, *R* cannot be easily found. However, if the magnitude of the edge response from two different size plates were divided by each other, then *R* would cancel along with $\sqrt{k}$, leaving only α unknown and therefore solvable. Putting the two measurements together yields the ratio *A*, which is defined as

$$A = \left|\frac{V_r^{(1)}(t)}{V_r^{(2)}(t)}\right| \left(\frac{\sqrt{d_1^{2w}}}{\sqrt{d_2^{2w}}}\right) = e^{\alpha\left(d_2^{2w} - d_1^{2w}\right)}. \tag{3-16}$$

This is second equation necessary for finding complex permittivity.

3.5.1 Simplified Extraction

Now that the necessary equations have been defined, in order to compute complex permittivity in a simple manner, one last assumption is made. This assumption uses the binomial expansion to find a closed form solution since $\varepsilon_r^{1/2}$ will not provide one.

$$(1+x)^n \approx 1+nx\ldots \; x<<1. \tag{3-17}$$

Applying this approximation to the relative permittivity in the propagation constant, *k*, yields

$$\varepsilon_r^{1/2} = (\varepsilon' - j\varepsilon'')^{1/2} = (\varepsilon')^{1/2}\left(1 - j\frac{\varepsilon''}{\varepsilon'}\right)^{1/2} \approx (\varepsilon')^{1/2}\left(1 - j\frac{\varepsilon''}{2\varepsilon'}\right)^{1/2} \approx \sqrt{\varepsilon'} - j\frac{\varepsilon''}{2\sqrt{\varepsilon'}}. \tag{3-18}$$

Therefore,

$$\begin{aligned} \mathrm{Im}(\varepsilon_r^{1/2}) &\approx -\frac{\varepsilon''}{2\sqrt{\varepsilon'}} \\ \mathrm{Re}(\varepsilon_r^{1/2}) &\approx \sqrt{\varepsilon'} \end{aligned} \tag{3-19}$$

which implies that

$$\begin{aligned} \alpha &= -k_0\,\mathrm{Im}(\varepsilon_r^{1/2}) \approx -k_0\left(-\frac{\varepsilon''}{2\sqrt{\varepsilon'}}\right) \approx \frac{k_0\varepsilon''}{2\sqrt{\varepsilon'}}. \\ \beta &= k_0\,\mathrm{Re}(\varepsilon_r^{1/2}) \approx k_0\sqrt{\varepsilon'} \end{aligned} \tag{3-20}$$

Substituting (3-20) into (3-14) and (3-16) gives

$$\begin{aligned} t_{2w} &= \frac{d_{2w}}{v_p} = \frac{d_{2w}}{\omega/\beta} = \frac{\beta d_{2w}}{\omega} \approx \frac{k_0\sqrt{\varepsilon'}d_{2w}}{\omega} \\ \frac{\ln(A)}{d_2^{2w} - d_1^{2w}} &= \alpha \approx \frac{k_0\varepsilon''}{2\sqrt{\varepsilon'}} \end{aligned} \tag{3-21}$$

which can be manipulated to solve for the relative complex permittivity with the solution for ε' given as

$$\varepsilon' = \left(\frac{\omega t_{2w}}{k_0 d_{2w}} \right)^2 \tag{3-22}$$

and ε'' given as

$$\varepsilon'' \approx \frac{2\sqrt{\varepsilon'}\ln(A)}{k_0\left(d_2^{2w} - d_1^{2w}\right)}. \tag{3-23}$$

3.6 Summary

This chapter has laid out a process for setting up and calibrating a rectangular waveguide probe. Furthermore, frequency range considerations were presented in order to prevent the generation of "higher order" modes in the parallel plate region of the probe setup. The effect of this is seen when applied to Plexiglas samples in Chapter 4. Two signal processing methods were also discussed, and both are used in the following chapter. Finally, the extraction technique was developed based upon the formulation from Chapter 2. The results from using this technique are presented in Chapter 4.

4. Analysis and Results

This chapter takes the method laid out in Chapter 3 and presents the data gathered from using this method on two Plexiglas samples. First, the uncertainty associated with the measurements is analyzed so that confidence intervals for the final extraction of permittivity can be determined. Then the results of the two signal processing methods discussed in Chapter 3 are presented. Finally, the permittivity extraction technique is applied to the data, and results are presented.

4.1 Error Analysis

The material characterization technique developed in this research will have some degree of error associated it. Understanding this error is important in being able to assess the method's accuracy and effectiveness.

Before the uncertainty of the relative complex permittivity can be computed, the sources of error must be identified. The formulas in (3-21) provide the basis for identifying these error terms. Of these values, four are variable and must be measured. One of these, the variable representing distance from the center of the aperture to the edge and back , d_{2w}, is determined by using calipers to measure the flange plates. The other three (angular frequency, ω, two way time, t_{2w}, and the ratio of response amplitudes, A) are measured by the NWA, and two of these (t_{2w} and A) are derived through the Fourier analysis accomplished by the NWA.

The NWA utilizes averaging and IF bandwidth to reduce measurement noise level. Since the value *A* is a ratio, and the signal processing will apply similar mathematical mechanisms on the signal, the effect of the uncertainty in *A* is assumed to be negligible.

4.1.1 Time and Frequency as Variables

The manual [3] lists the minimum frequency-domain resolution for the NWA as 1Hz. This resolution is assumed to be the worst case uncertainty for a frequency measurement. Given that the frequency step size is several orders of magnitude greater than the uncertainty, it is assumed this uncertainty is negligible.

The time-domain uncertainty consists of two parts. The first is drawn from the frequency uncertainty. However, because the frequency uncertainty is considered negligible, this part of the time-domain uncertainty is also considered negligible.

Fourier analysis provides the second form of time-domain uncertainty which has a larger effect. Equation (3-5) shows that the time-domain resolution is dependent on the bandwidth. Therefore, it is possible that the actual edge reflection lies within the irresolvable region. However, it is assumed that this edge reflection peak is closer to the point that is identified as the edge reflection than any other point. This means that the actual response, *x*, will lie somewhere within an area of $-T_s/2 \le x \le T_s/2$ where T_s is the temporal resolution. This area is centered on the point that is identified as the edge reflection. Furthermore, since the actual edge reflection is not dependent on the Fourier analysis but on the material under test, it could theoretically occur anywhere within area defined above with equal probability. Therefore, the probability density function (PDF) of the time of occurrence for the edge reflection can be defined as a unit step function [1].

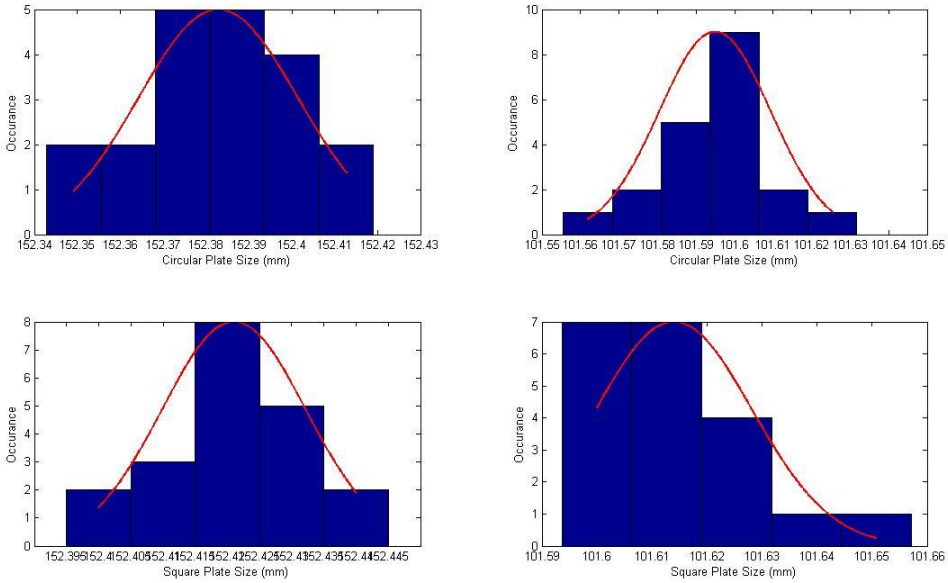

Figure 4-1: The histograms and associated Gaussian curves for the measurement plates

This means that the standard uncertainty, *u*, for the time of occurrence of the edge reflection can be defined as

$$u = \frac{T_s}{2\sqrt{3}}. \tag{4-1}$$

4.1.2 Distance as a Variable

The two way distance for each flange plate was measured using precision calipers. A sample of 20 measurements per plate was taken in order to be able to form a good statistical picture. The plates were found to exhibit a Gaussian, or normal, PDF with a low standard deviation. The distributions of the selected plates with an overlaid Gaussian curve are shown in Figure 4-1. The statistical information, shown in Table 4-1, forms the basis of the uncertainty associated with distance in the extraction formulas.

Table 4-1: Statistical data generated from 20 sample measurements of each plate that was used in taking measurements.

	Mean (mm)	Standard Deviation (mm)
6” Circular Plate	152.38	0.0186
4” Circular Plate	101.59	0.0145
6” Square Plate	152.42	0.0112
4” Square Plate	101.61	0.0142

4.1.3 Overall Uncertainty

As shown in the previous sections, both the uncertainty in the distance traveled by the wave in the parallel plate system and the uncertainty of the time variable resolution have the most significant effect on the results of the permittivity extraction. Therefore, the uncertainty of both must be taken into account during the permittivity extraction. For the real part of the relative complex permittivity, uncertainty can be computed as [13], [15]

$$\delta\varepsilon'(d,t) = \frac{\partial\varepsilon'(d_0,t_0)}{\partial d}\delta d + \frac{\partial\varepsilon'(d_0,t_0)}{\partial t}\delta t \tag{4-2}$$

with d and t being the distance and time variables, the subscript 0 denotes the expected values and the δ denotes the uncertainty. The imaginary part of the relative complex permittivity is defined similarly, as

$$\delta\varepsilon''(d_1,d_2,\varepsilon') = \frac{\partial\varepsilon''(d_{1_0},d_{2_0},\varepsilon'_0)}{\partial d_1}\delta d_1 + \frac{\partial\varepsilon''(d_{1_0},d_{2_0},\varepsilon'_0)}{\partial d_2}\delta d_2 + \frac{\partial\varepsilon''(d_{1_0},d_{2_0},\varepsilon'_0)}{\partial\varepsilon'}\delta\varepsilon' \tag{4-3}$$

where d_{1_0} and d_{2_0} are the expected values for d_1 and d_2 respectively and ε_0' is the expected value for ε'.

4.2 Results of Data Processing

Before the data can be used in calculations to find the relative complex permittivity, it must first be processed using one of the methods detailed in Chapter 3. Each method carries with it benefits and drawbacks. However, the overall extent of the drawbacks remains unknown until the extraction is accomplished and can be compared against known values. As a preliminary measure of effectiveness, each figure shown below will have a marker showing the ideal location of the edge response using the industry standard value of 2.6 for the real part of relative complex permittivity.

4.2.1 Kaiser Windowing

As a processing method, Kaiser windowing presents an attractive option, especially since the NWA has the ability to perform the windowing on the data. It is able to suppress the sidelobes of the signals so that weaker signals, like the edge reflection, can be more readily identified. However this comes at a cost of spreading the waveforms of the responses as shown in Figure 3-9. The figures below present time domain data that has been taken from 5.55mm and 4.39mm thick samples of Plexiglas. A frequency ranges were 10.0 GHz to 16 .0GHz and 10.0 GHz to 18.5 GHz respectively. The thicker sample has a reduced frequency range to avoid exciting the 1st order mode. The Kaiser window was applied using the NWA with a β value of 6 with zero padding. Data was taken using the 4" and 6" circular plates. As a frame of reference, each figure below also has data using the same setup without the Kaiser window plotted with it.

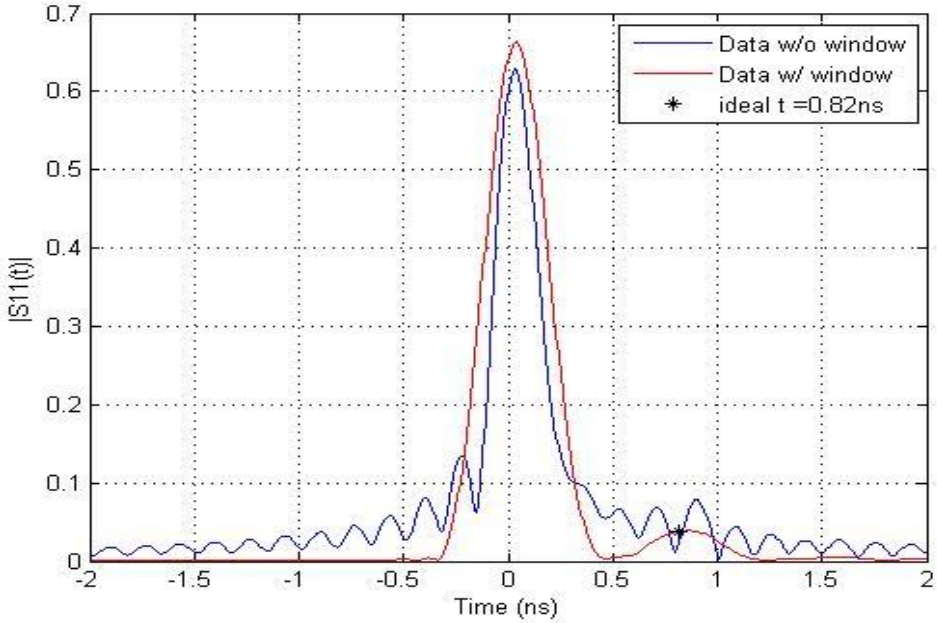

Figure 4-2: Data from the 6" circular plate measuring a 5.55mm thick sample

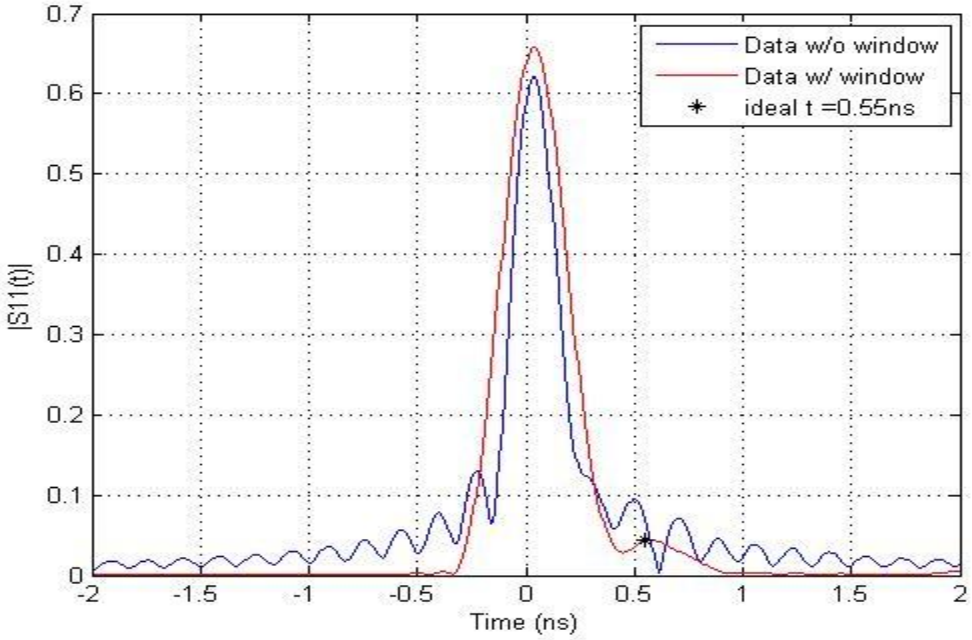

Figure 4-3: Data from the 4" circular plate measuring a 5.55mm thick sample

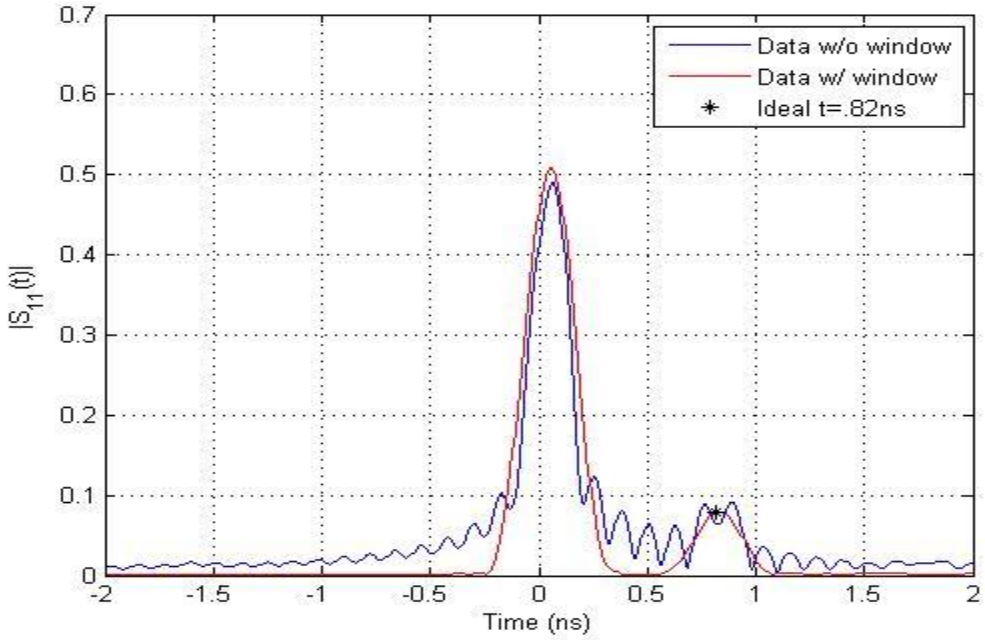

Figure 4-4: Data from the 6" circular plate measuring a 4.39mm thick sample

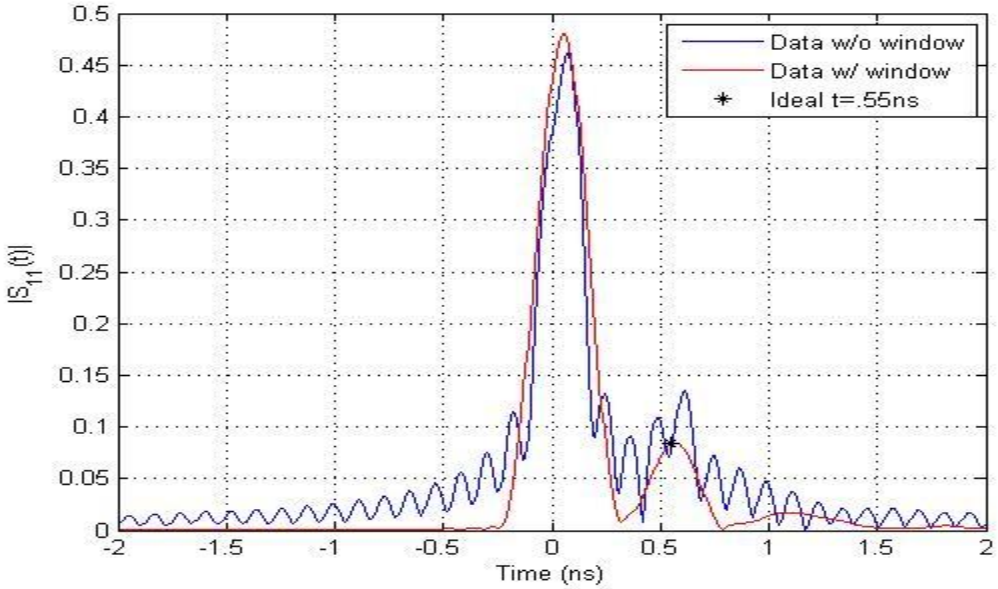

Figure 4-5: Data from the 4" circular plate measuring a 4.39mm thick sample

As is evident from the figures above, the ideal reflection point is slightly off from the identified peak of each edge reflection. The actual edge reflection times for the 6" plate and the 4" flange plate are .86ns and .57ns respectively for the thick sample and .83ns and .56ns respectively for the thin sample.

4.2.2 Signal Subtraction

Signal subtraction has the benefit of isolating the signal and does not broaden the responses. However, the effectiveness of the subtraction depends heavily on the quality of the initial approximation of the 0^{th} order response. For this research, a 3rd order polynomial fit was chosen based upon heuristic examinations of the frequency-domain data and how well the transformed fit removed the 0^{th} order reflection. The figures below present time-domain data from the measured samples. Both a 5.55mm and a 4.39mm thick sample of Plexiglas were used. The frequency ranges were 10.0 GHz to 16.0 GHz and 10.0 GHz to 18.5 GHz respectively. Again, the thicker sample has a reduced frequency range to avoid exciting the 1^{st} order mode. The data covers the 6" and 4" plates of square and circular geometry. Zero padded data uses a 1601 point zero pad. Once again, as a frame of reference, the original data collected from the NWA is included in each figure.

As a final note, the algorithm used to process the data designated the largest response remaining after the signal processing as the edge reflection. The only case in which a large response may be ruled out is if it occurred before the time at which the reflection could have happened in free space. The reason for this is to evaluate the method assuming no a priori knowledge of the material's relative complex permittivity.

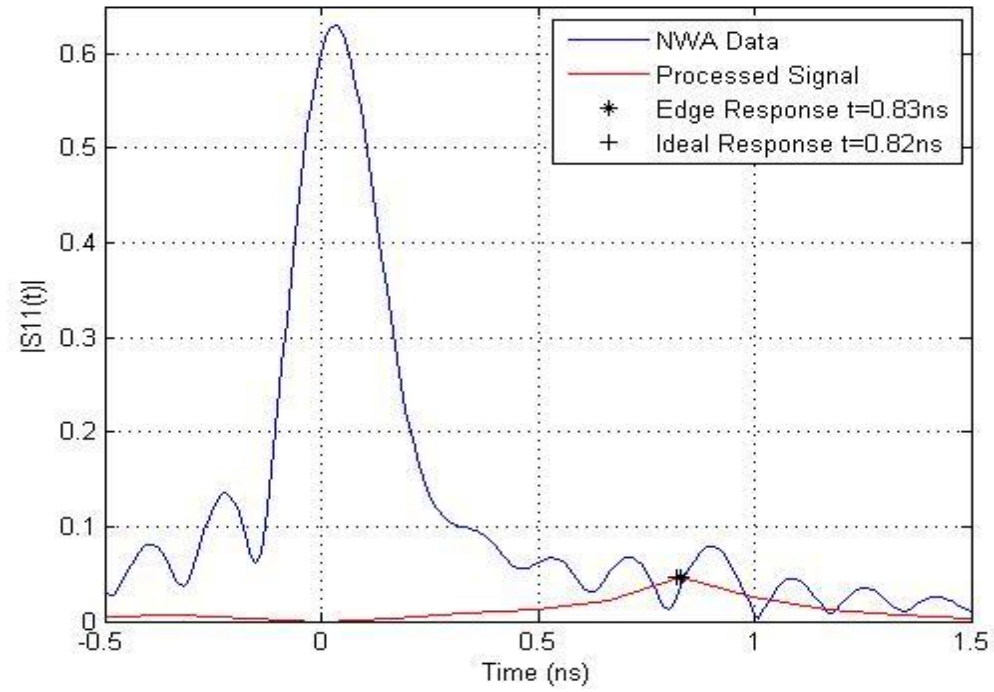

(a)

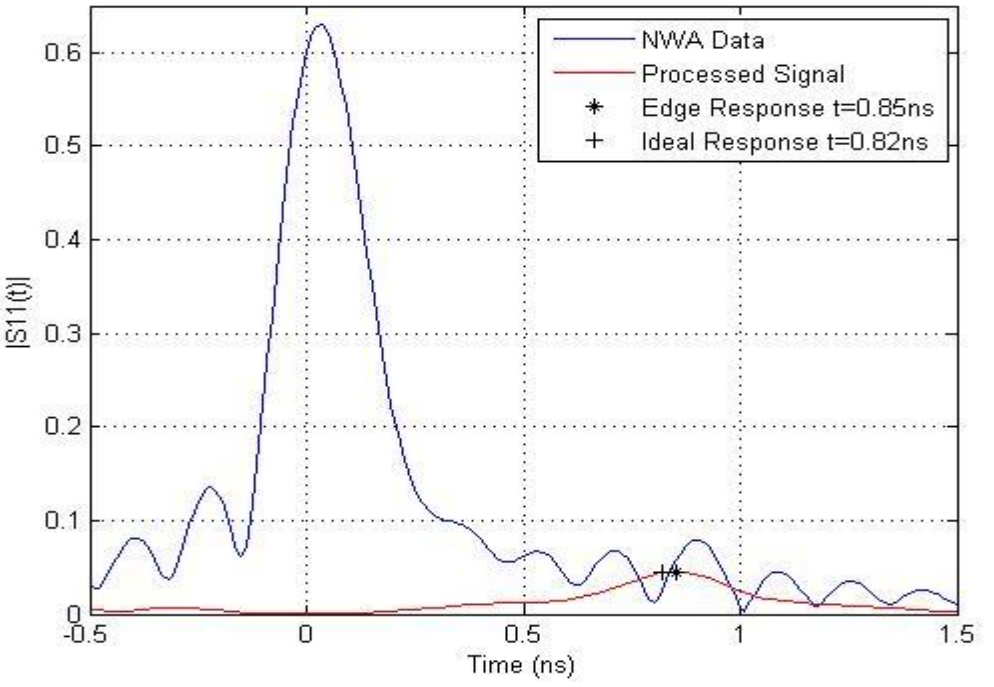

(b)

Figure 4-6: (a) Non zero padded and (b) zero padded edge responses for a 6" circular plate measuring a 5.55mm thick sample

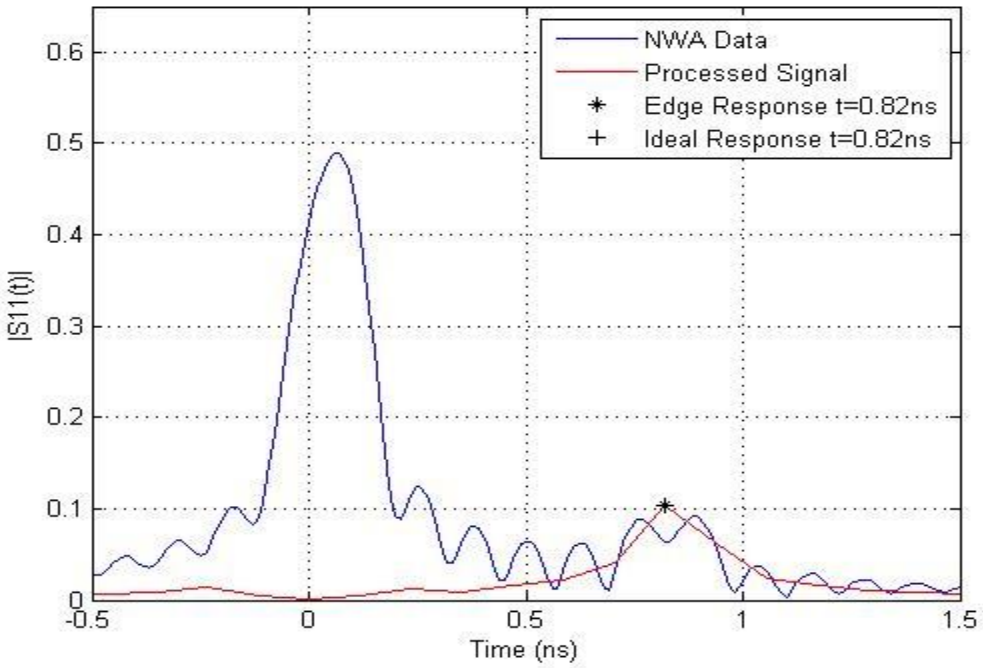

(a)

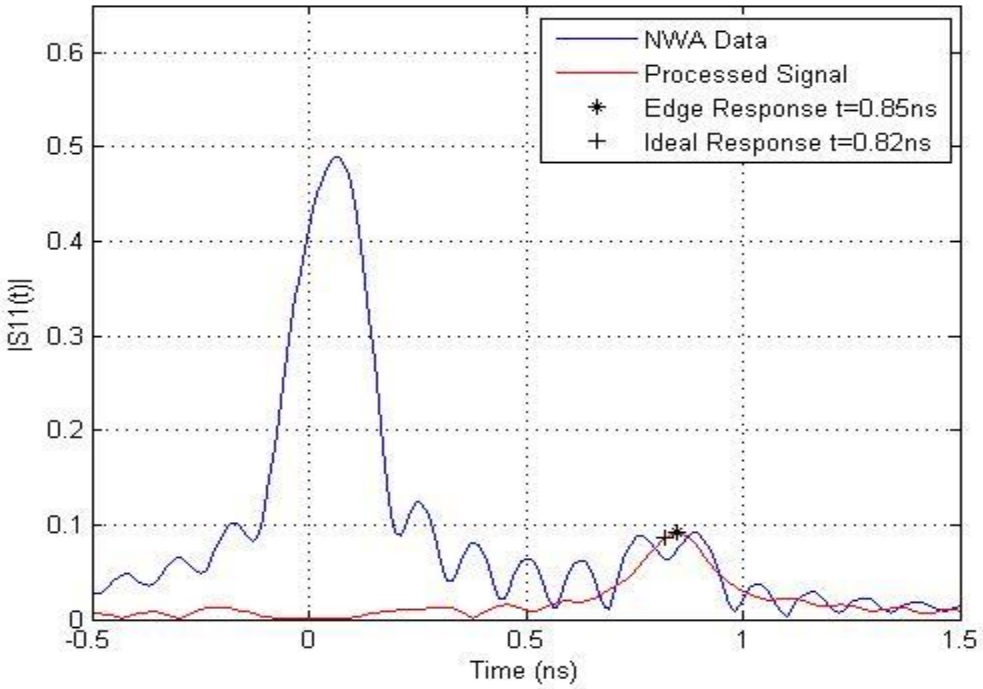

(b)

Figure 4-7: (a) Non zero padded and (b) zero padded edge responses for a 6" circular plate measuring a 4.39mm thick sample

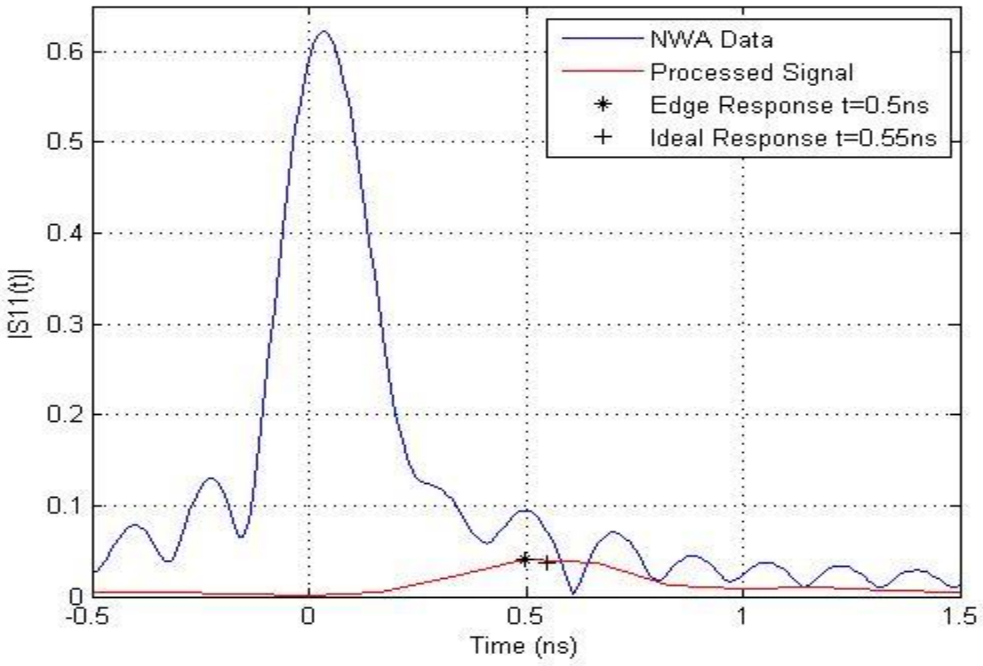

(a)

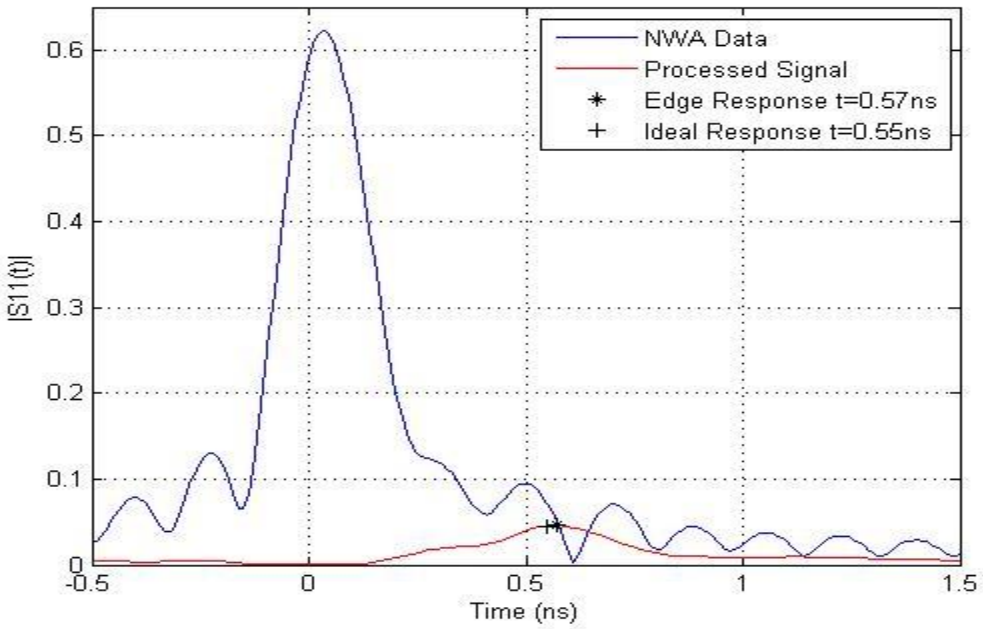

(b)

Figure 4-8: (a) Non zero padded and (b) zero padded edge responses for a 4" circular plate measuring a 5.55mm thick sample

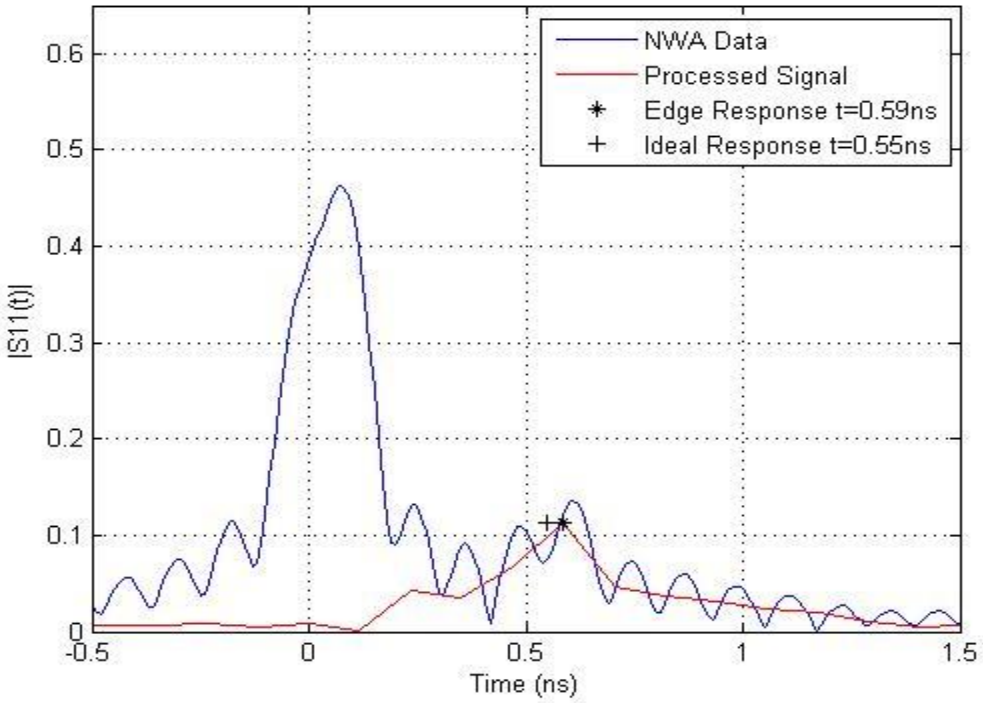

(a)

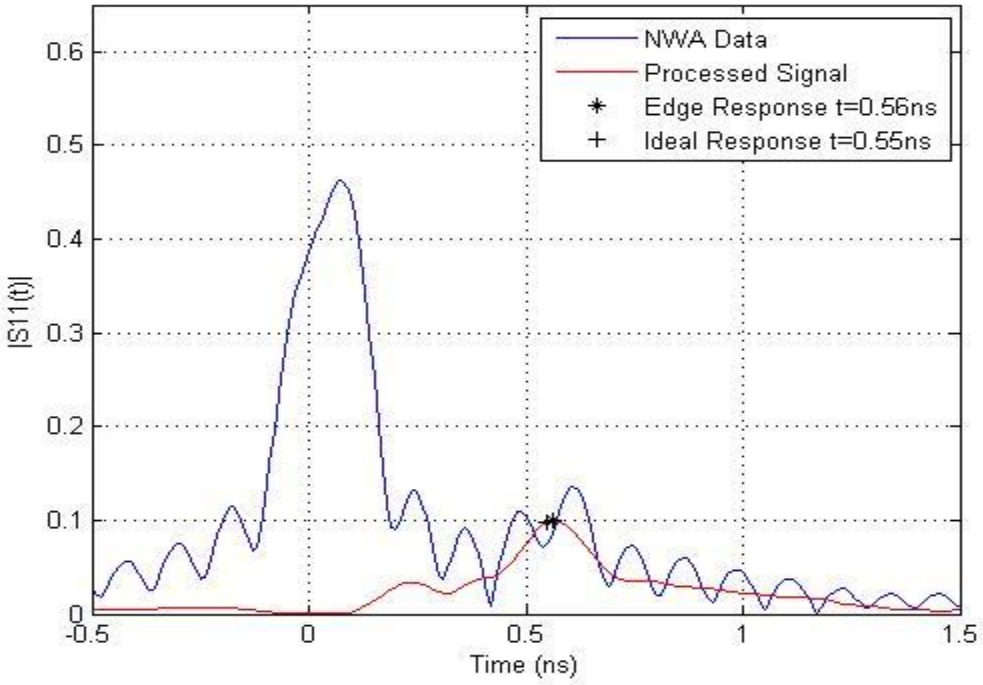

(b)

Figure 4-9: (a) Non zero padded and (b) zero padded edge responses for a 4" circular plate measuring a 4.39mm thick sample

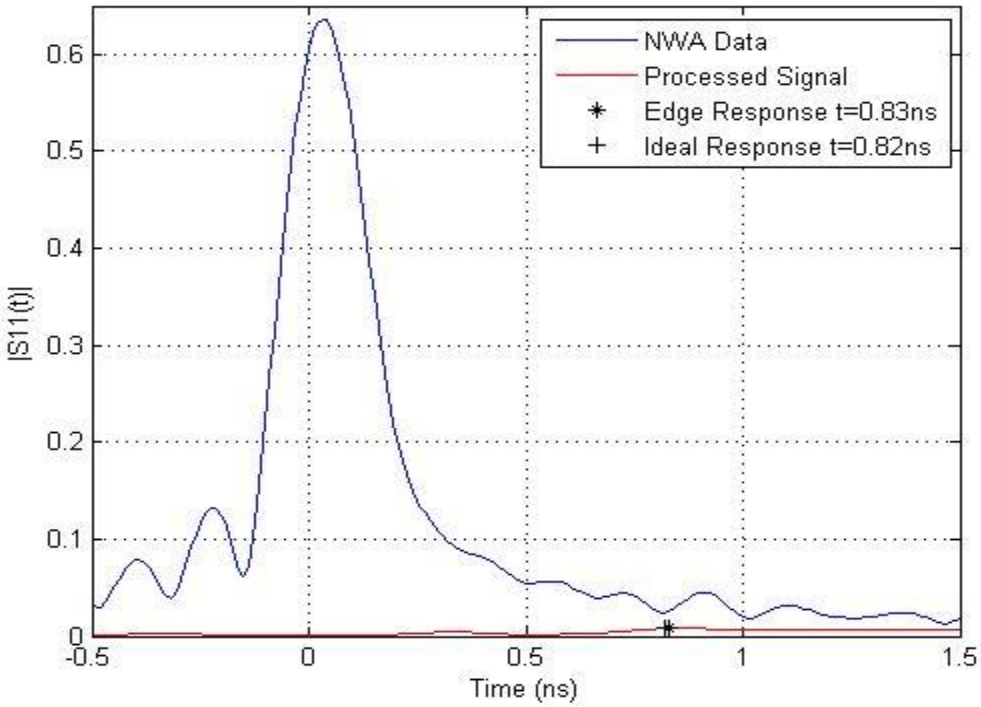

(a)

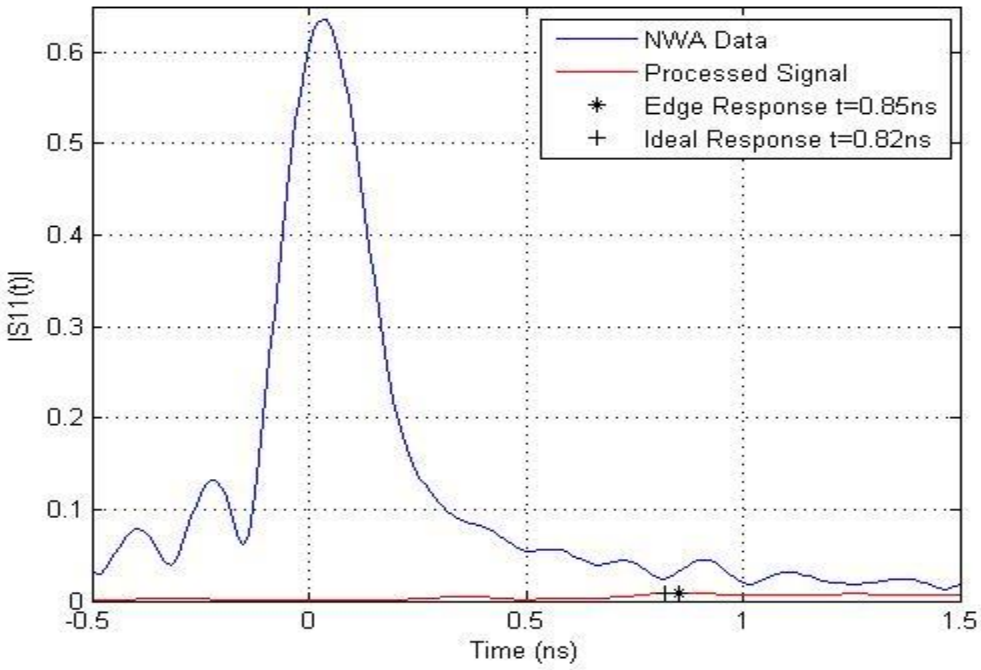

(b)

Figure 4-10: (a) Non zero padded and (b) zero padded edge responses for a 6" square plate measuring a 5.55mm thick sample

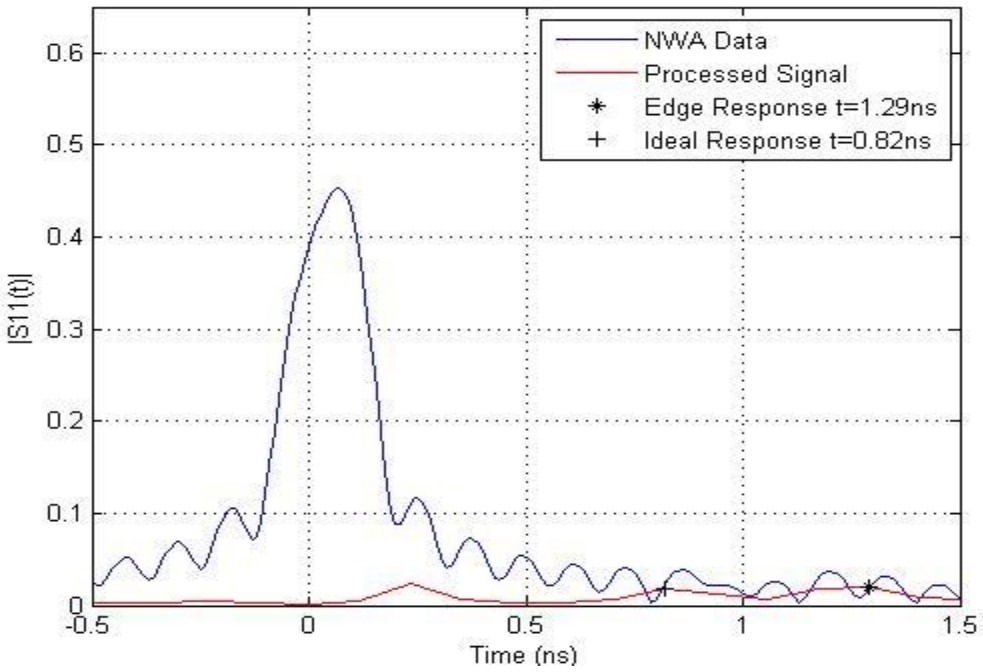

(a)

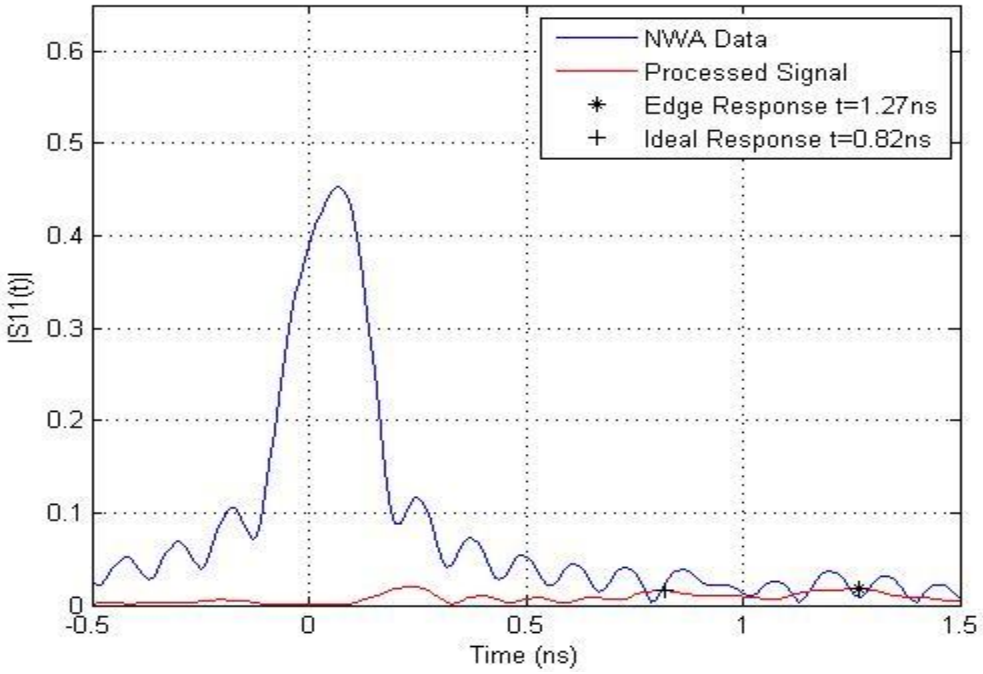

(b)

Figure 4-11: (a) Non zero padded and (b) zero padded edge responses for a 6" square plate measuring a 4.39mm thick sample

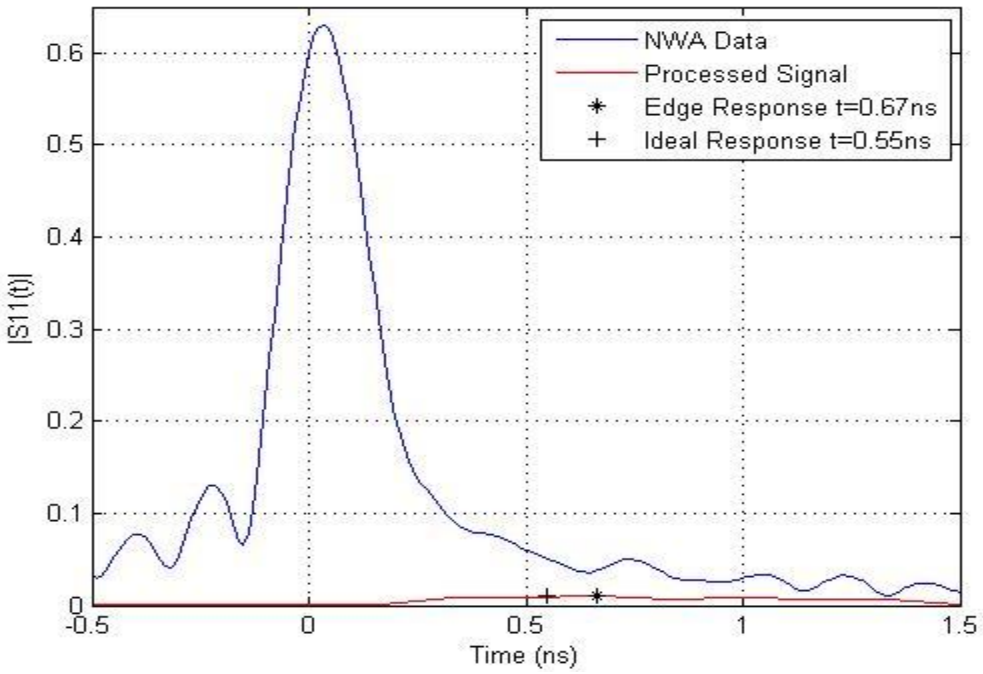

(a)

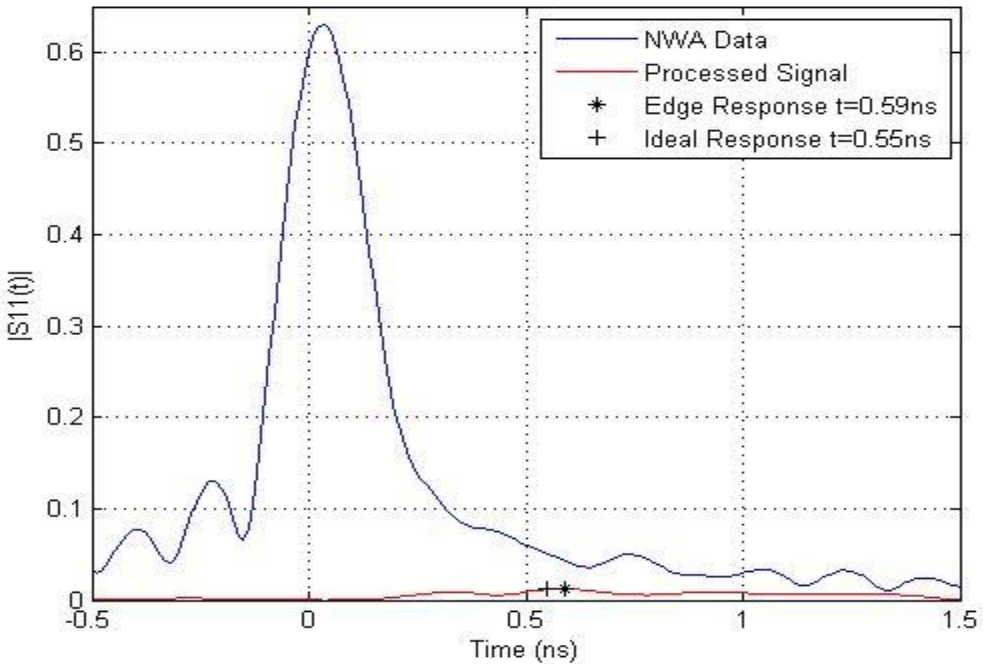

(b)

Figure 4-12: (a) Non zero padded and (b) zero padded edge responses for a 4" square plate measuring a 5.55mm thick sample

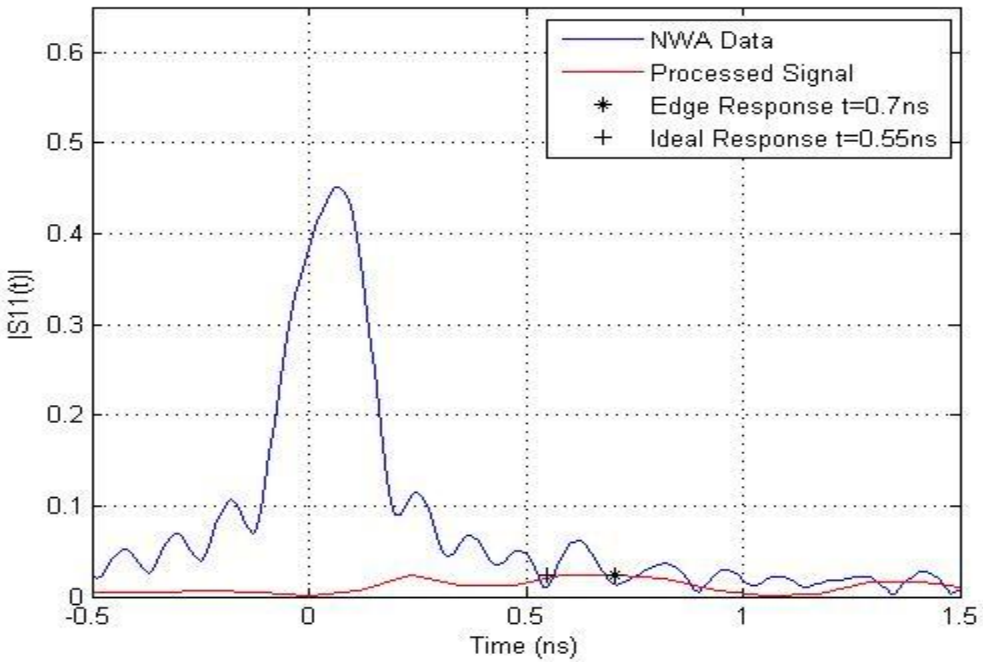

(a)

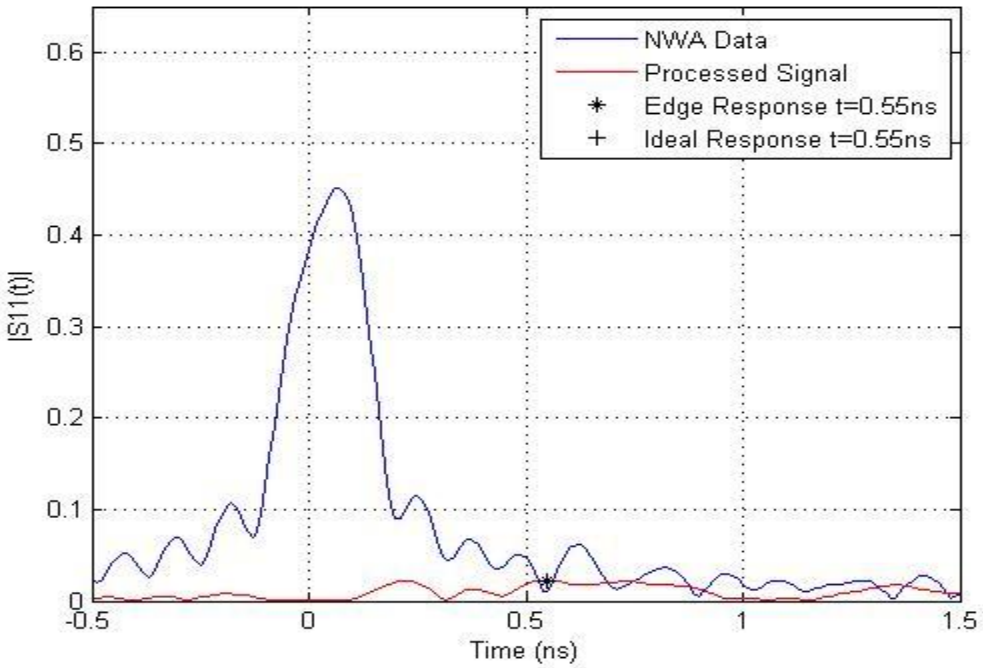

(b)

Figure 4-13: (a) Non zero padded and (b) zero padded edge responses for a 4" square plate measuring a 4.39mm thick sample

For the circular plates, the signal subtraction method works very well in indentifying the edge reflection. The thicker samples provide less accurate data. The zero padding provides no distinct advantage in identifying the edge reflection. The method was not effective when square flange plates were used. As is seen in the above figures, the square flange plates had responses that were widely dispersed making accurate identification of the edge reflection difficult.

The table below gives a summary all of the reflection times and amplitudes from each of the figures above. These values will be used in calculating the relative complex permittivity.

Table 4-2: All the edge response times, the difference of the response times from the ideal, and the amplitudes for each measurement setup processed using the signal subtraction method

		Zero Pad	Time (ns)	Diff from Ideal (ns)	Amplitude
6" circular	Thick Sample	N	0.831	0.011	0.0471
		Y	0.851	0.031	0.0456
	Thin Sample	N	0.821	0.001	0.1026
		Y	0.849	0.029	0.0913
4" circular	Thick Sample	N	0.499	-0.047	0.0406
		Y	0.574	0.028	0.0459
	Thin Sample	N	0.587	0.041	0.1133
		Y	0.562	0.016	0.0989
6" square	Thick Sample	N	0.831	0.011	0.0089
		Y	0.851	0.031	0.0085
	Thin Sample	N	1.291	0.471	0.0199
		Y	1.267	0.447	0.0181
4" square	Thick Sample	N	0.665	0.119	0.0100
		Y	0.592	0.046	0.0122
	Thin Sample	N	0.704	0.158	0.0243
		Y	0.549	0.003	0.0221

4.3 Final Extraction

After the edge reflections have been identified via one of the two signal processing methods addressed previously, the data can be used to calculate the relative complex permittivity for the sample material. The data will be presented against industry standard values of ε' and ε'' for Plexiglas which are defined here as $\varepsilon' = 2.6$ and $\varepsilon'' = 0.0150$ [12]. The sample materials used for these measurements were a 5.55mm and a 4.39mm thick sample of Plexiglas. Frequency ranges were 10.0 GHz to 16.0 GHz and 10.0 GHz to 18.5 GHz respectively. As previously mentioned, the thicker sample has a reduced frequency range to avoid exciting the 1st order mode. Both the 6" and 4" square and circular plates were used to take measurements.

4.3.1 Simplified Extraction

The equations for the simplified extraction were detailed in (3-22) and (3-23). In calculating the uncertainty for (3-22), using (4-2) yields

$$\delta\varepsilon' = \left(\frac{-2c^2 {t_{2w_0}}^2}{{d_{2w_0}}^3} \right) \delta d + \left(\frac{2c^2 t_{2w_0}}{{d_{2w_0}}^2} \right) \delta t \tag{4-4}$$

where d_{2w_0} is the expected value for the distance and t_{2w_0} is the expected value for time. The uncertainty for (3-23) based on (4-3) yields

$$\delta\varepsilon'' \approx -\frac{2\sqrt{\varepsilon'}\ln(A)}{k_0\left(d_{1_0}^{2w} - d_{2_0}^{2w}\right)^2}\delta d_2^{2w} + \frac{2\sqrt{\varepsilon'}\ln(A)}{k_0\left(d_{2_0}^{2w} - d_{1_0}^{2w}\right)^2}\delta d_1^{2w} - \frac{2\ln(A)}{k_0\sqrt{\varepsilon'}\left(d_{2_0}^{2w} - d_{1_0}^{2w}\right)}\delta\varepsilon'. \tag{4-5}$$

4.3.1.1 Kaiser Windowing

The results from applying a simple extraction to data from the NWA that has been processed using Kaiser windowing are displayed in Figure 4-14 and Figure 4-15. It is observed that ε' falls within two standard deviations (i.e., 95% confidence assuming a Gaussian distribution). ε'' is within confidence intervals in the thicker sample; however, because the thicker sample has a reduced bandwidth, the uncertainty for ε' is greater.

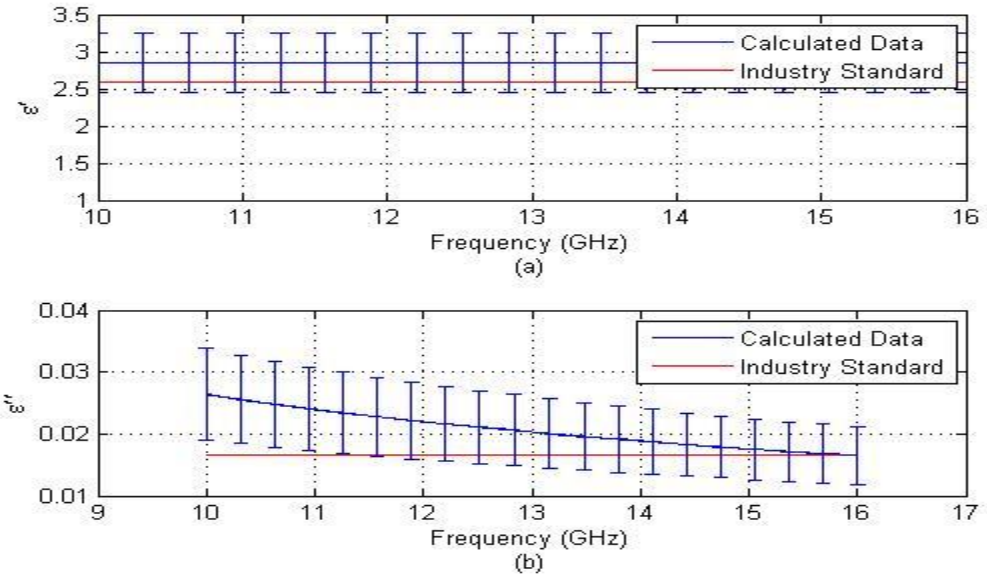

Figure 4-14: ε_r of a 5.55mm sample of Plexiglas using the simplified extraction and processed with Kaiser windowing.

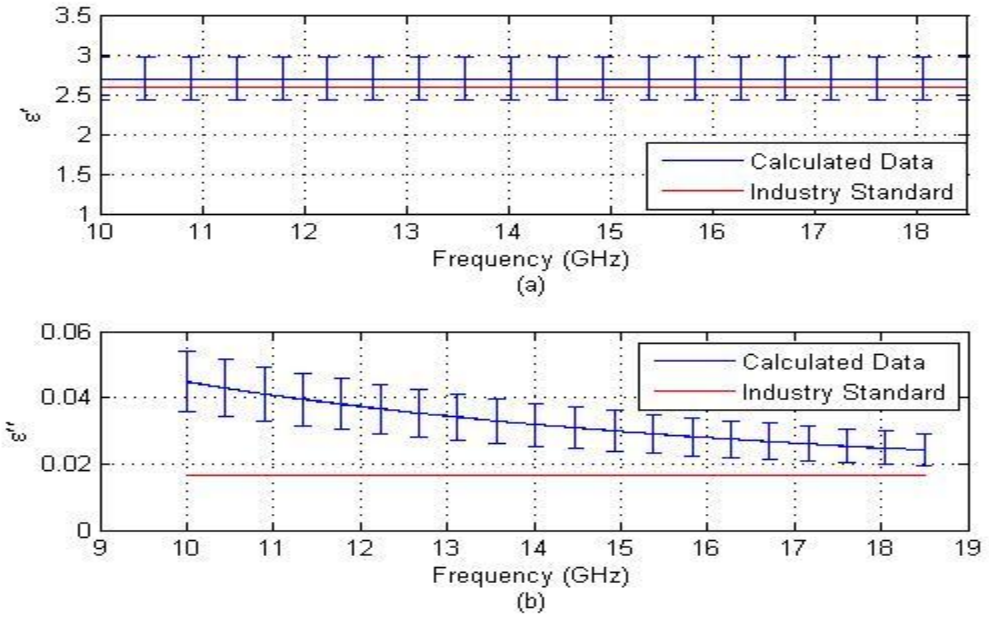

Figure 4-15: ε_r of a 4.39mm sample of Plexiglas using the simplified extraction and processed with Kaiser windowing.

4.3.1.2 Signal Subtraction

With the edge reflections identified from data that has been processed using the signal subtraction method, a simple extraction can be performed. The extracted data covers both a 5.55mm and a 4.39mm thick sample of Plexiglas. Frequency ranges were 10.0GHz to 16.0GHz and 10.0GHz to 18.5GHz respectively. The thicker sample required a reduced frequency range in order to avoid exciting the 1st order mode in the parallel-plate region. The probe setup used both the square and circular geometries. The extracted results are presented below.

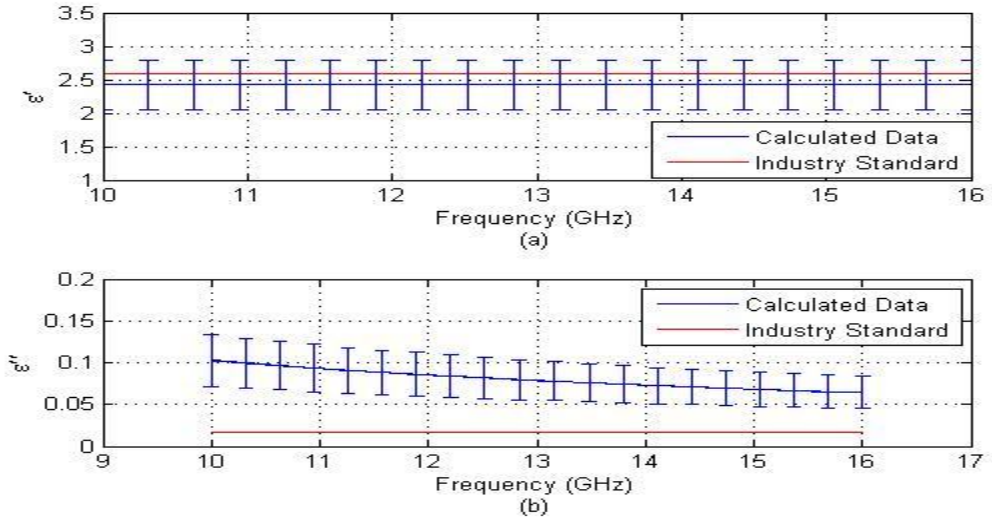

Figure 4-16: ε_r for a 5.55mm thick sample of Plexiglas using circular plates with no zero padding

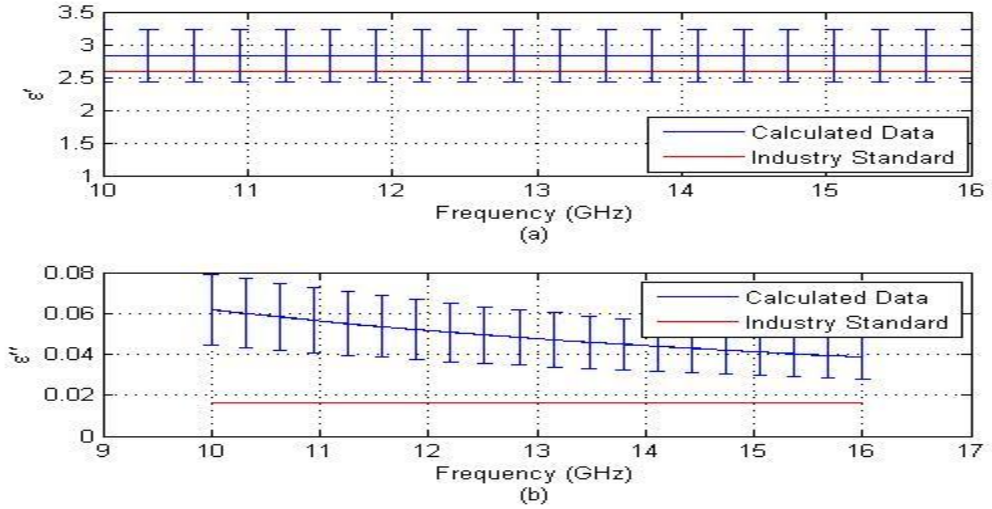

Figure 4-17: ε_r for a 5.55mm thick sample of Plexiglas using circular plates with zero padding

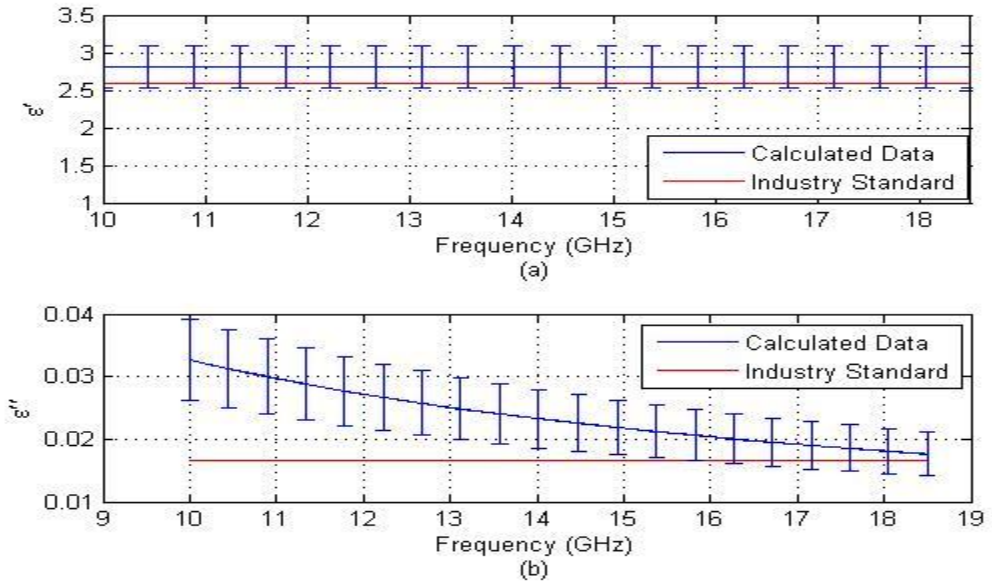

Figure 4-18: ε_r for a 4.39mm thick sample of Plexiglas using circular plates with no zero padding

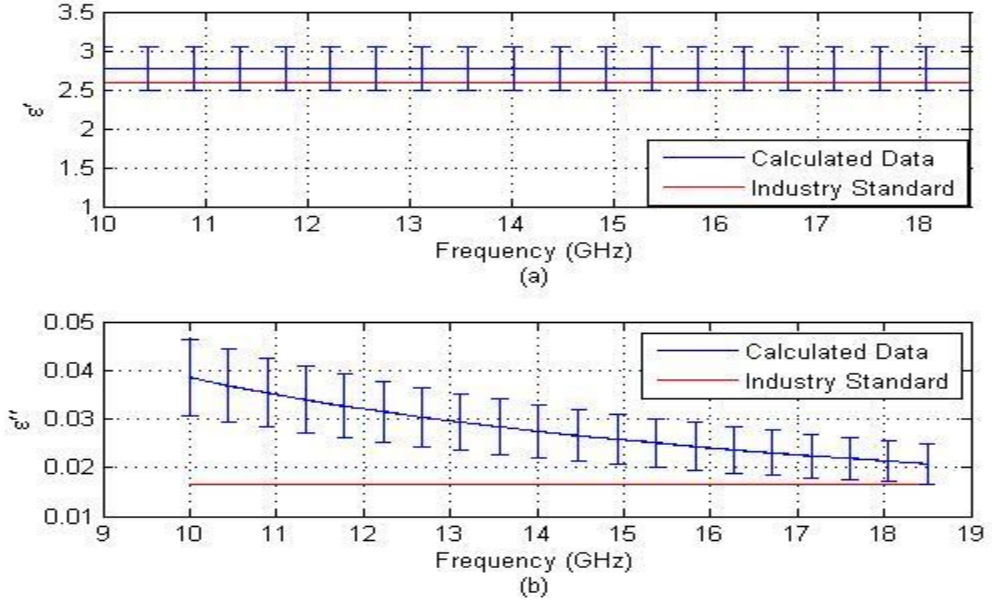

Figure 4-19: ε_r for a 4.39mm thick sample of Plexiglas using circular plates with zero padding

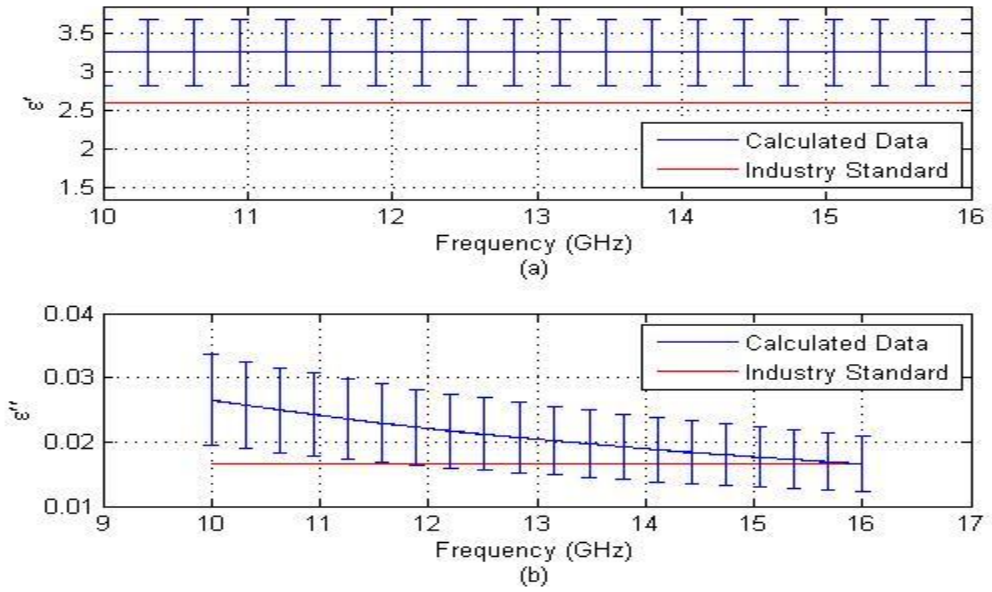

Figure 4-20: ε_r for a 5.55mm thick sample of Plexiglas using square plates with no zero padding

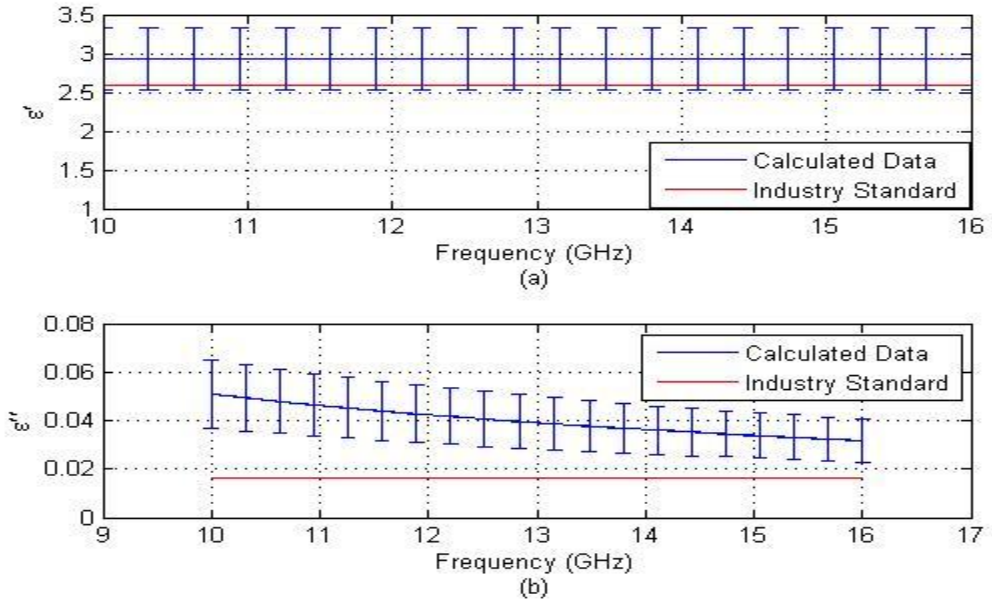

Figure 4-21: ε_r for a 5.55mm thick sample of Plexiglas using square plates with zero padding

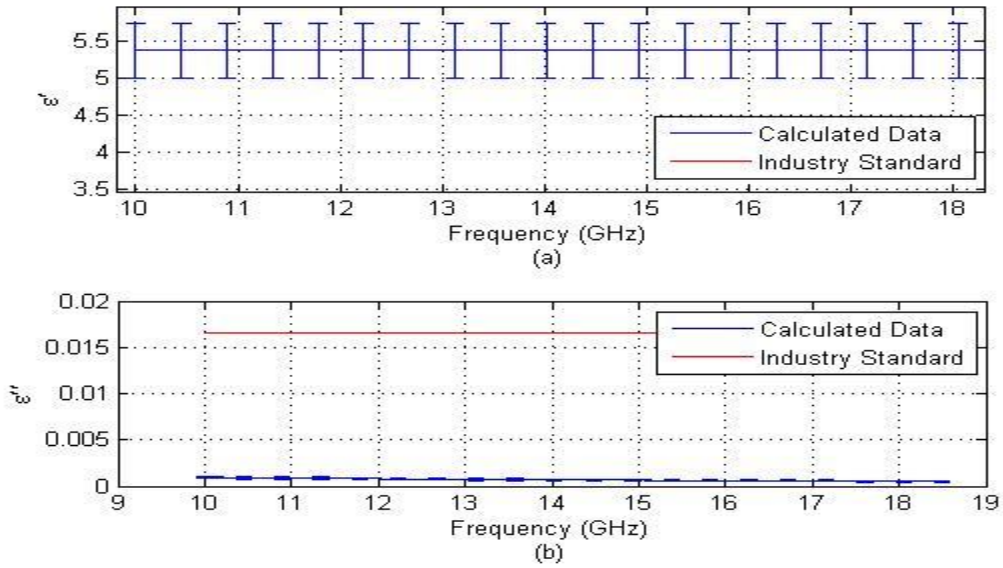

Figure 4-22: ε_r for a 4.39mm thick sample of Plexiglas using square plates with no zero padding

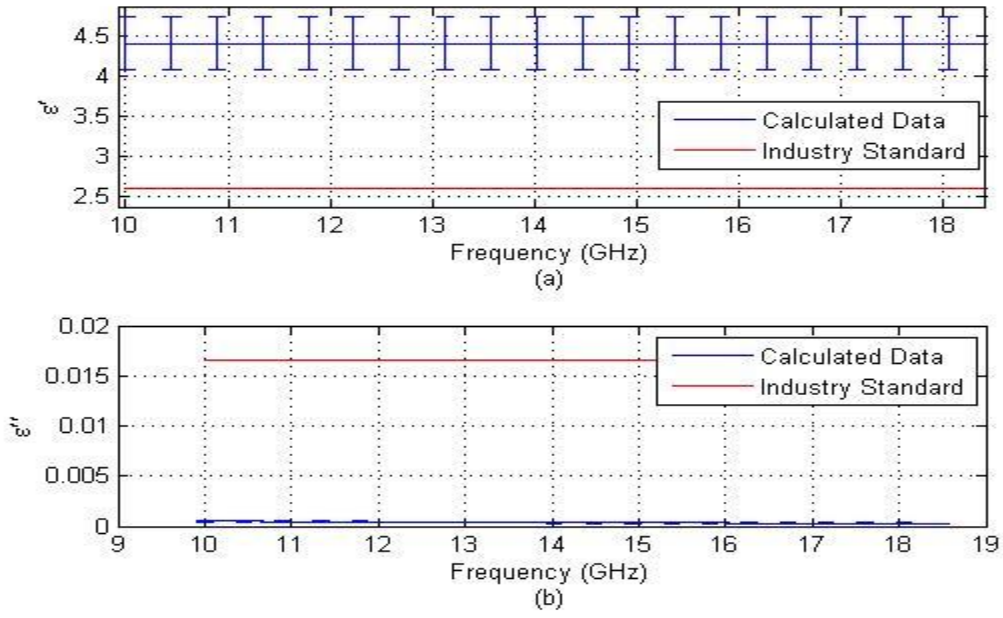

Figure 4-23: ε_r for a 4.39mm thick sample of Plexiglas using square plates with zero padding

Examining the figures above, when using square flange plates, the data for the real part of ε_r is almost twice the industry standard. In some applications, this may be an acceptable tolerance; however, in most, it is not. In contrast, the circular flange plate data is all within 95% confidence intervals. In the best case, the uncertainty is only ±0.28, which is considered an acceptable tolerance for many industry applications.

With the assumption of a low loss material, the imaginary part of ε_r, in contrast to the real part, can be a multiple of the industry standard and still be considered within tolerances (dependent on application) as long as it is within the same order of magnitude. From this perspective, the circular flange plate measurements appear to be good. However, they are most accurate using the thin Plexiglas sample with no zero padding. When examining the averaged ε' and ε'', the same observations hold true. This data is contained in Table 4-3 where the averaged ε' and ε'' are presented along with the industry standard as a reference.

Table 4-3: All averaged ε´ and ε´´ data from each measurement along with the industry standards for those values.

Sig Process	plate	Sample Size	Zero Pad	Avg ε´	Avg ε´´	Ind Std ε´	Ind Std ε´´
Kaiser	Circular	5.55mm	N/A	2.846	0.021	2.6	0.015
		4.39mm	N/A	2.699	0.032	2.6	0.015
Signal Subtraction		5.55mm	N	2.42	0.080	2.6	0.015
			Y	2.834	0.049	2.6	0.015
		4.39mm	N	2.805	0.023	2.6	0.015
			Y	2.768	0.028	2.6	0.015
	Square	5.55mm	N	3.261	0.021	2.6	0.015
			Y	2.927	0.040	2.6	0.015
		4.39mm	N	5.381	0.001	2.6	0.015
			Y	4.414	0.000	2.6	0.015

4.4 Summary

This Chapter has presented the results of using a simple time domain based extraction of complex permittivity that utilizes the edge reflections from waveguide probes. Starting with an examination of the uncertainty associated with the system, the signal processing methods were discussed, and the results of the processing were used in extracting the permittivity. Two samples were used for the measurements, a 5.55mm thick and a 4.39mm thick sample of Plexiglas. Furthermore, the frequency range covered for the measurements was 10.0GHz to 16.0GHz and 10.0GHz to 18.5GHz respectively. Two types of probes were used for taking the measurements. The first type was a Ku-band waveguide with either a 6" or 4" square flange plate attached. The second type was also a Ku-band waveguide with either a 6" or 4" circular flange plate attached. It was found zero-padding did not affect the final results when using the signal subtraction method. Furthermore, the results when using circular flange plates are considered to be acceptable for use in most industry applications. Finally, higher order modes should be avoided so that the 8.5GHz bandwidth of the Ku-band waveguide can be used. Since temporal resolution was the primary driver of uncertainty, avoiding a reduced bandwidth in the Ku-band waveguide will lead to more accurate measurements with the desired confidence intervals.

5. Conclusions and Recommendations

A simple method has been developed that can produce reasonable results for extracting relative complex permittivity from a low-loss, non-magnetic, non-dispersive dielectric. Plexiglas was used in this research as a proof-of-concept, but the method can be applied to other materials within this classification. The main advantage of the method is that it is both non-destructive and computationally simple. This is of huge benefit over other non-destructive methods that often use a Method of Moments solution which can be time consuming and computationally demanding. Furthermore, since the method is non-destructive, no time is lost in sample preparation, and no errors are introduced by a poorly fitted sample.

5.1 Conclusions

During the development of this method, two measurement setups and two signal processing methods were explored as a means of accomplishing the measurement and analyzing the signal. This was done intentionally so that the method could be further refined in later work without needing determinations to be made regarding plate geometries or signal processing.

5.1.1 Preferred Plate Geometry

Based on the results presented Chapter 4, plate geometry appears to have a profound effect on the real part of the relative complex permittivity. This effect is caused because the 1st order reflection may no longer be considered the edge reflection in square flange plates. While 2nd order reflections at about the appropriate times are noticed,

positive identification cannot be made since the permittivity is assumed to be unknown. Therefore the circular plates are the preferred geometry for use with this method.

5.1.2 Preferred Signal Analysis Method

Unlike the plate geometry, the final extracted data does not unequivocally show one signal processing method to be superior to another. The average for ε' for Kaiser windowing (with zero padding) is higher than the averages obtained via signal subtraction, but when comparing Figure 4-14 to Figure 4-16, the values for ε' are within 95% confidence intervals. However, waveform spreading occurs when using Kaiser windowing, which subsequently diminishes temporal resolution. Therefore, Signal Subtraction is identified as the preferred signal processing method. Furthermore, the NWA used in this research was able to apply the Kaiser window which added to the simplicity of the method. Other NWA's may not possess this capability which removes the key benefit of using that signal processing method.

5.1.3 Confidence Interval

The temporal resolution uncertainty was based on the assumption that there was a uniform probability for the 1st order reflection to occur somewhere within an interval that is the size of the resolution and centered on the point indentified as the measured edge response. This is a valid assumption if $\boldsymbol{\varepsilon_r}$ is unknown for the sample material. Therefore, the exact location of the edge reflection remains unknown and, subsequently, has an equal chance of being anywhere within the region identified with the edge response. This leads to an uncertainty in the ε' measurement of ±0.28 when using a 95% confidence interval and the full frequency range of the Ku-band waveguide. However, the PDF can be altered from a unit step function to another form that may better describe the material

if there is some a priori knowledge of the material. With an altered PDF, the uncertainty can be reduced leading to increased precision.

5.1.4 Final Recommendation

Based upon the recommendations made above, the method described in this research can be optimized in the following ways. First, circular flange plates should be used to reduce ambiguity associated with identifying the edge reflection. Additionally, since temporal resolution significantly affects the uncertainty in the measurement, anything that will reduce the bandwidth of the system (such as having to lower the upper limit of the frequency range in order to avoid generating high order modes) should be avoided. Finally, the signal subtraction method of signal processing should be used to avoid waveform broadening and loss of temporal resolution.

However, even with this setup, the method is not without drawbacks. Because of the inherent simplicity of the system, material type is limited to a certain form of dielectrics. Furthermore, uncertainty is introduced into the measurement via the signal processing and the assumptions made in order to keep the calculations computationally simple.

5.2 Recommendations for Future Research

Research should be conducted into increasing the bandwidth of the measurement apparatus. With increased bandwidth, the time resolution would be improved which would lead to more precise and accurate measurements. Another area for future research is to looking into somewhat more rigorous mathematical models. As another research area, the signal subtraction method, which relies on a simple polynomial fit, should

explore the use of Hermite or Legendre polynomials. Additional signal processing research should also focus on the use of other windows as effective signal processing methods. The Kaiser window was considered to be representative of similar windows (Hann, Hamming, etc), but without a formal study, the other windows cannot be ruled out as effective signal processing methods. A final area to investigate is expanding or modifying the method to include magnetic materials.

Appendix A: Acronyms

Bandwidth	BW
Discrete Fourier Transform	DFT
Electromagnetic	EM
Fourier Transform	FT
Gigahertz	GHz
Inverse Fast Fourier Transform	IFFT
Network Analyzer	NWA
Nicholson Ross Weir	NRW
Nano-second	ns
Perfect Electrical Conducting/Perfect Electric Conductor	PEC
Probability Density Function	PDF
Short-Open-Load-Thru	SOLT
Thru-Line-Reflect	TRL

Appendix B: Plate Drawings

This section includes the drawings used by the AFIT machine shop to fabricate the plates that were used to form the waveguide probes, they are included here as a reference in case plates need to be fabricated again in the future.

6” Circular plate

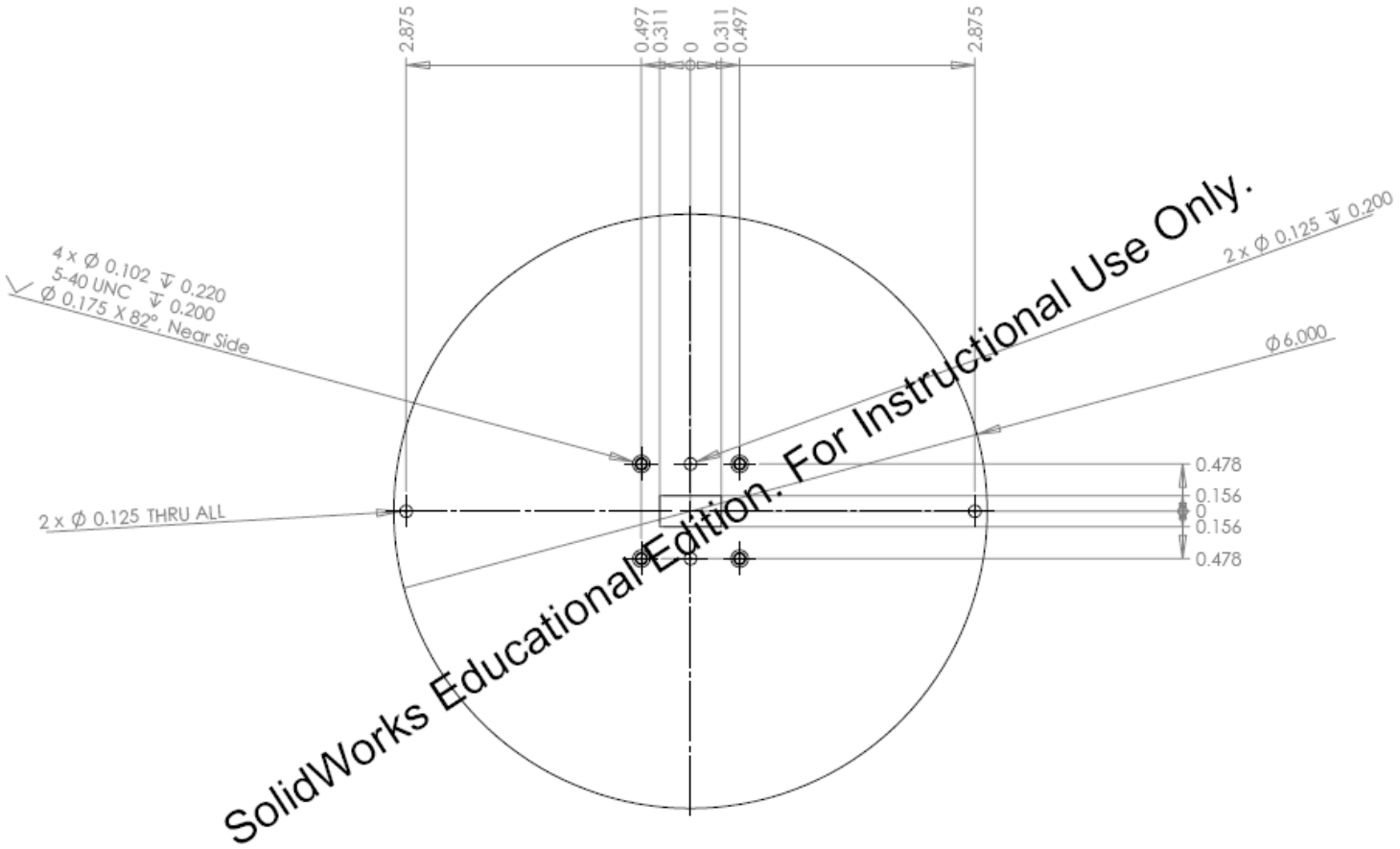

4” Circular Plate

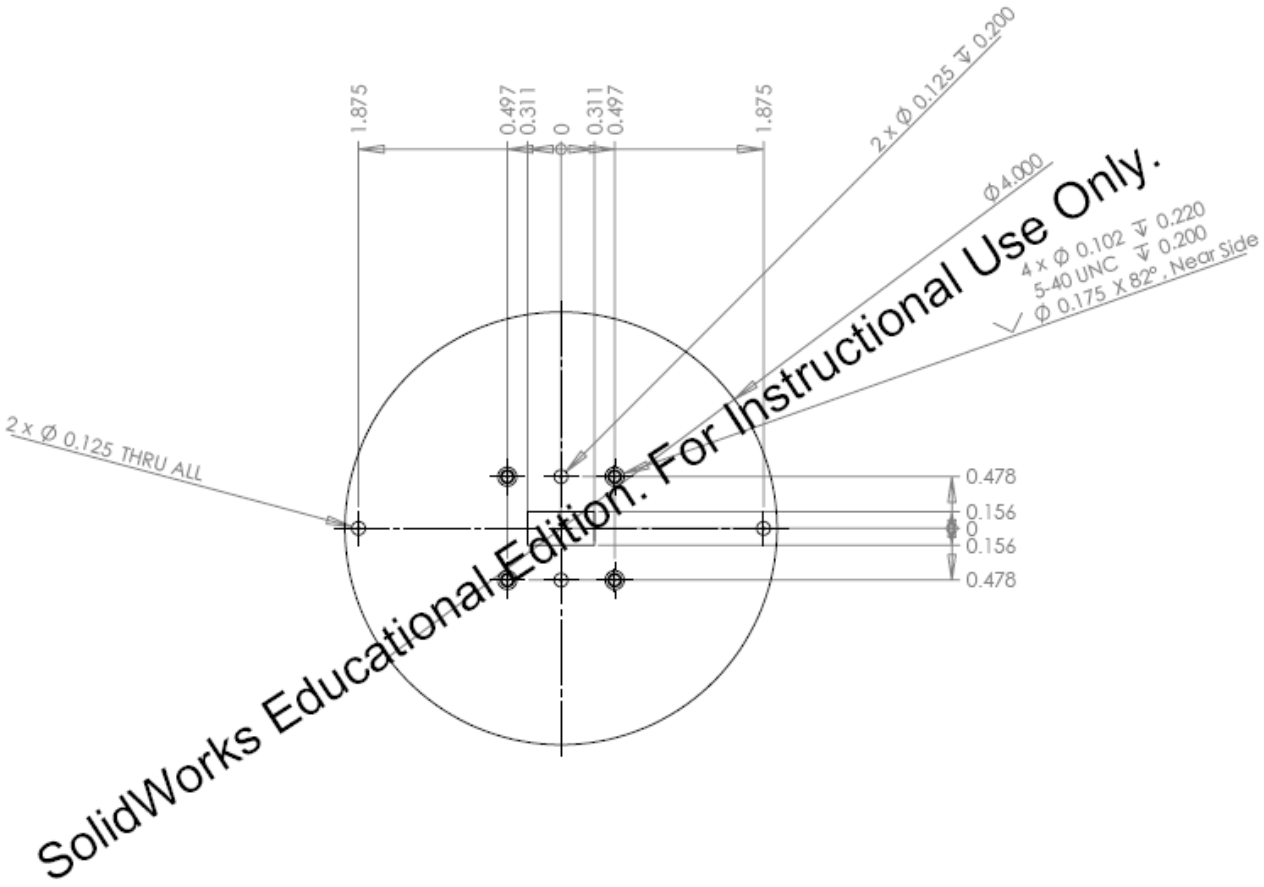

6” Square Plate

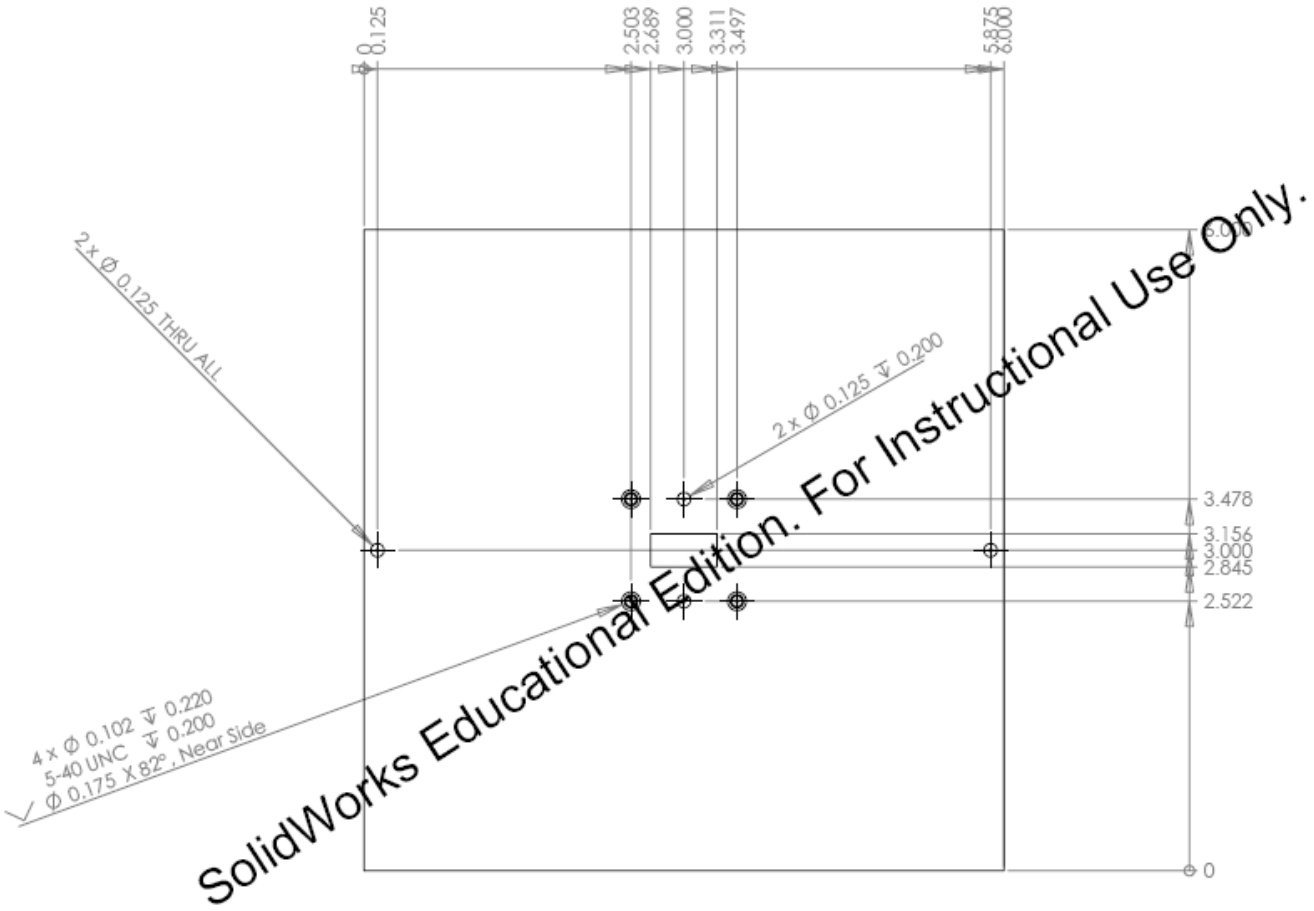

4” Square Plate

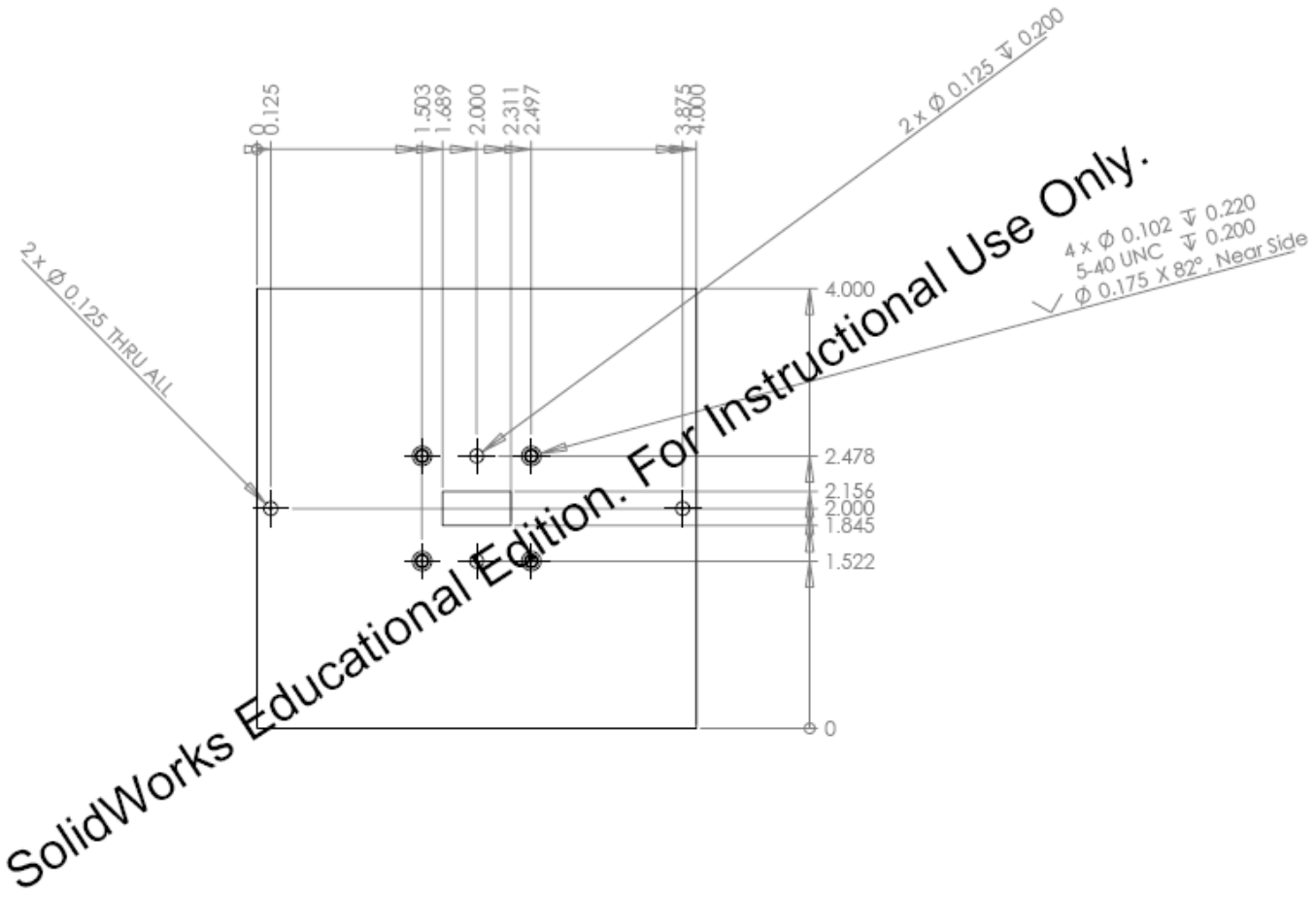

Appendix C: Waveguide Bandwidth

A Ku-band waveguide was used as part of the probe setup. The operating bandwidth used was 10.0GHz to 18.5GHz. That bandwidth was determined based upon the following calculations.

Whereas the parallel plate system relied on operating in the 0^{th} order mode, a wave guide requires at least the 1^{st} order mode to be able to excite waves. For purposes of this application, the TE_{10} mode was used. Therefore, the bandwidth of the system is dependent on two factors. The first is TE_{10} mode cutoff. Frequencies below this threshold will not excite waves inside the waveguide and will, therefore, be useless. This defines the low point for the bandwidth. The high point is defined by the TE_{20} cutoff frequency. This point is chosen so that no higher order modes are excited. The formula for the cutoff frequency for a TE_{mn} mode of a freespace filled waveguide is given by Balanis [4] as

$$f_c = \frac{c}{2\pi}\sqrt{\left(\frac{m\pi}{a}\right)^2 + \left(\frac{n\pi}{b}\right)^2} \qquad (5\text{-}1)$$

where *a* and *b* represent the width and height of the aperture waveguide respectively. For a Ku-band waveguide, those dimensions are 0.311" and 0.622".

When calculated, the cutoff frequency for the TE_{10} mode is 9.49GHz, and the cutoff frequency for the TE_{20} mode is 18.975GHz. Typically, the lower bound is multiplied by 1.25 and the upper bound by 0.95 in order to ensure that the waveguide is operating only in the range of the desired mode. For a Ku-Band waveguide, this is usually defined as approximately 12GHz to 18GHz. However, since bandwidth is vitally important to this method, a compromise was made in order to expand the bandwidth beyond the 6GHz covered by the traditionally defined

range. This compromise settled on using a range from 10GHz to 18.5GHz. Theoretically, the boundaries could be expanded to cover 9.5GHz to 18.9GHz; however, this would introduce a risk of higher order modes corrupting the data.

Bibliography

[1] A. Leon-Garcia, *Probability, Statistics, and Random Processes for Electrical Engineering*, 3rd Ed. Upper Saddle River, NJ: Pearson education, Inc, 2008.

[2] A.M. Nicolson and G.F. Ross. "Measurement of the Intrinsic Properties of Materials by Time-domain Techniques," *IEEE Transactions on Instrumentation and Measurement*, IM-19:377–382, Nov 1970.

[3] Agilent Technologies, "Agilent PNA Series Network Analyzer," Printed Version of PNA Help User's and Programming Guide, June 2010.

[4] C. A. Balanis, *Advanced Engineering Electromagnetics*, New York: John Wiley & Sons, 1989.

[5] G. Hanson and A. Yakovlev, *Operator Theory for Electromagnetics: An Introduction*, Springer-Verlag, New York, 2001.

[6] L. F. Chen, C. K. Ong, C. P. Neo, V. V. Varadan, and V. K. Varadan, *Microwave Electronics Measurement and Materials Characterization*, New York: John Wiley & Sons, 2004.

[7] M. W. Hyde, "Determining the resistivity of resistive sheets using transmission measurements," M.S. thesis, Air Force Institute of Technology, Wright-Patterson Air Force Base, Ohio, 2006.

[8] M.W.Hyde et al., "Nondestructive electromagnetic material characterization using a dual waveguide probe: A full wave solution," *Radio Sci*., 44, RS3013, doi:10.1029/2008RS003937.

[9] M. W. Hyde and M. J. Havrilla, "Measurement of Complex Permittivity and Permeability Using Two Flanged Rectangular Waveguides," *Microwave Symposium, 2007. IEEE/MTT-S International* , pp.531-534, 3-8 June 2007.

[10] N Geckinli and D.Yavuz , "Some novel windows and a concise tutorial comparison of window families," *Acoustics, Speech and Signal Processing, IEEE Transactions on* , vol 26, no 6, pp. 501- 507, Dec 1978.

[11] R.E. Collin, *Field Theory of Guided Waves*, 2nd Ed., Piscataway, N.J., IEEE Press, 1991.

[12] R. F. Harrington, *Time-Harmonic Electromagnetic Fields*, New York: IEEE Press, 2001.

[13] R. G. Fehlen, "Air gap error compensation for coaxial transmission line method of electromagnetic material characterization," M.S. thesis, Air Force Institute of Technology, Wright-Patterson Air Force Base, Ohio, 2004.

[14] S. Haykin and B. Van Veen, *Signals and Systems,* 2nd Ed. New York: John Wiley & Sons, 2003.

[15] S. P. Dorey, "Stepped waveguide electromagnetic material characterization technique," M.S. thesis, Air Force Institute of Technology, Wright-Patterson Air Force Base, Ohio, 2004.

[16] W.B. Weir, "Automatic Measurement of Complex Dielectric Constant and Permeability at Microwave Frequencies," IEEE Proceedings, volume 62, 33–36. Jan 1974.

REPORT DOCUMENTATION PAGE

Form Approved
OMB No. 074-0188

1. REPORT DATE *(DD-MM-YYYY)*	2. REPORT TYPE	3. DATES COVERED *(From – To)*
24-03-2011	Master's Thesis	Sept 2009 – March 2011

TITLE AND SUBTITLE

A Simple Non-Destructive Method for Characterizing Non-Dispersive, Low-Loss Dielectrics

5a. CONTRACT NUMBER

5b. GRANT NUMBER

5c. PROGRAM ELEMENT NUMBER

6. AUTHOR(S)

Olney, Thomas S., Captain, USAF

5d. PROJECT NUMBER
11G170

5e. TASK NUMBER

5f. WORK UNIT NUMBER

7. PERFORMING ORGANIZATION NAMES(S) AND ADDRESS(S)
Air Force Institute of Technology
Graduate School of Engineering and Management (AFIT/ENG)
2950 Hobson Way, Building 640
WPAFB OH 45433-8865

8. PERFORMING ORGANIZATION REPORT NUMBER

AFIT/GE/ENG/11-31

9. SPONSORING/MONITORING AGENCY NAME(S) AND ADDRESS(ES)
Mr. Garrett Stenholm
Air Force Research Lab
2591 K St Bldg 254
Wright Patterson AFB, OH 45433-7602
Garrett.stenholm@wpafb.af.mil
DSN 785-9179

10. SPONSOR/MONITOR'S ACRONYM(S)
AFRL/RYS

11. SPONSOR/MONITOR'S REPORT NUMBER(S)

12. DISTRIBUTION/AVAILABILITY STATEMENT
This material is declared a work of the U.S. Government and is not subject to copyright protection in the United States. Approved for public release; Distribution Unlimited.

13. SUPPLEMENTARY NOTES

14. ABSTRACT

It is shown how permittivity can be extracted via time domain reflection data from a perfect electric conductor (PEC) backed planar sample of a low-loss, non-dispersive dielectric using two rectangular Ku-band waveguide aperture probes with attached PEC flange plates of the same geometry but different dimensions. Of critical importance is being able to identify the reflection from the edge of the flange plate in the parallel plate region created by the plate and the PEC backing of the sample. A signal processing method that takes advantage of physical insight into the geometry and superposition is developed for identifying this edge reflection.

Measurements are taken using a square and circular plate geometries. The data gathered is processed using both Kaiser windowing and the signal subtraction method developed in this research. Final results are presented with determinations made about how to optimize the method.

15. SUBJECT TERMS
Rectangular Waveguide Probe, Material Measurement, Permittivity, Dielectrics

16. SECURITY CLASSIFICATION OF:			17. LIMITATION OF ABSTRACT	18. NUMBER OF PAGES	19a. NAME OF RESPONSIBLE PERSON
a. REPORT	b. ABSTRACT	c. THIS PAGE			Dr. Michael Havrilla ENG
U	U	U	UU	89	19b. TELEPHONE NUMBER *(Include area code)* (937) 255-6565, ext 7252 (Michael.Havrilla@afit.edu)

Standard Form 298 (Rev. 8-98)
Prescribed by ANSI Std. Z39-18